Studies on Diagnostics of Laser Produced Sn Plasmas for Extreme Ultraviolet Light Source Using Collective Thomson Scattering

佐藤, 祐太

Studies on Diagnostics of Laser Produced Sn Plasmas for Extreme Ultraviolet Light Source Using Collective Thomson Scattering

Yuta Sato

Contents

Chapter 1

Introduction

1.1Background

Lithography is a key technology in the semiconductor industry for improving performance of semiconductor integrated circuit. The performance has been improved by shortening the wavelength of the lithography light source because the light source wavelength plays an important role in determining the patterning resolution. The imaging performance of the projection optical system is evaluated by Rayleigh's equation. Resolution R (half pitch) of photo lithography is expressed as:

$$R = k_1 \frac{\lambda}{NA} \tag{1.1}$$

where k_1 is constant, λ is wavelength, and NA is numerical aperture. R can be reduced by increasing NA, decreasing k_1 factor, and decreasing λ. A light source used currently is an ArF excimer laser with a wavelength of 193 nm. The immersion and multi-patterning technologies are improving the values of NA and k_1. However there are physical limitations for such technologies. The stepper, which is a device used in the process of photo lithography as shown in Fig. 1.1, consists of a light source, a condenser lens, a

mask, a reduction projection lens, a wafer, and a control stage. For the next generation of semiconductor manufacturing aimed at a node size of less than 7 nm, extreme ultraviolet (EUV) lithography at a wavelength of 13.5 nm is expected to be the most promising technology.[1][2] The practical application of EUV has many problems, and the biggest problem is that the output power has not reached the target value. For the EUV light source, a very powerful output (~1 kW) is required to secure the processing speed, that is, the throughput as the exposure equipment. The EUV band radiation is absorbed while propagating in the atmosphere and by elements of refractive optics.[3] Thus, EUV lithography must be operated in vacuum conditions and with optical elements reflecting EUV light sufficiently. The optical element uses Mo/Si multilayer mirror and its reflectance is 70% at the maximum.[4] Figure 1.2 shows a schematic diagram of EUV lithography.[5] Since eleven multilayer mirrors are used in EUV lithography, the EUV light reaching the wafer is about 2% of the light source output power.

Concepts and designs of EUV lithography were suggested in 1988 and examined experimentally in 1989 and 1990.[1][6][7] A synchrotron radiation was used as a light source of EUV for the studies, because single wavelength is required for optical lithography. However, a synchrotron needs high cost and large space therefore it was only used in experiments for the purpose of the evaluation of optical elements.

There are many studies utilizing laser produced plasma (LPP) and discharge generated plasma (DPP) as the EUV light source.[8][9][10][11][12][13] Both DPP and LPP create a high temperature several hundred thousand kelvins, which enables a short wavelength emission at 13.5 nm.[14] LPP is a technique of producing plasma by irradiating a laser to a target, and DPP is a method of generating plasma by high current pulse discharge. Figures 1.3(a) and (b) show schematic diagrams of DPP and LPP.[2] DPP has high

conversion efficiency (CE) from electric power to in-band EUV energy, but collection efficiency is not high because EUV light can be collected only in a small solid angle. In addition, the electrodes lifetime and debris mitigation were issues to be solved.

On the other hand, LPP does not use the electrode and can produce plasma at an isolated space. Therefore, collective efficiency is higher than DPP, and LPP reduces debris in an EUV light source device. In addition, LPP can realize a point light source by producing minute plasmas and is suitable for a lithography light source. The problem of LPP is low output power and CE.[15] The required EUV output power is greater than 250 W at intermediate focus (IF). A research reported that LPP can continuously supply IF power 40 W for 6 hours and 50 W for 1 hour in 2013.[16] LPP produced by Sn and CO_2 laser is currently the strongest candidate of EUV light source. As a target material for EUV light source, tin (Sn) and xenon (Xe) were considered to be an influential candidate.[17][18] Xe is cleaner than Sn, but its emission spectra is weaker than Sn. In order to achieve the requirement output power, Sn is the current common target materials for EUV light sources. A fresh surface of the target is demanded by high CE, therefore, Sn is used as droplets with small diameters of 26 μm. A pre-pulse laser which expands the small Sn target has been introduced to increase the EUV light source power.[19] The pre-pulse laser expands a small tin droplet, and a CO_2 laser irradiates when it reaches a size of approximately 300 μm in diameter,[20] and a CE of approximately 4% was confirmed using this approach.[21]

The CE from driving laser to EUV light used for lithography is determined by the laser absorption rate of the plasma, the conversion rate from the absorbed power to the radiation power, and the ratio of the EUV power to the total radiation energy. Since the wavelength peak emitted from the plasma is determined by the averaged ionic charge (Z),

it is important to control the electron temperature (T_e). Also, the light quantity greatly depends on the electron density (n_e). It was concluded that the optimum n_e and T_e of the EUV light source plasma are 10^{24}-10^{25} m^{-3} and 30-50 eV, respectively.[22] Diagnostic of light source plasma is indispensable in order to realize the optimum EUV light source indicated by the theoretical model. However, direct measurements of these parameters of EUV light source plasmas, whose conversion efficiency is sufficiently high for practical use, have never been performed.

There are several studies which measured the Sn plasma parameters so far.[23][24] Kieft and colleagues estimated the electron density by Sn's Stark broadening measurement[25] and measured the time change of electron density and electron temperature of the discharge generated Sn plasmas by laser Thomson scattering (LTS) method.[26][27] In the research by Kieft *et al*., electron features of collective Thomson scattering were measured, but the plasma disturbance by the probing laser was a serious problem.

Simultaneous measurement of the n_e, T_e, and Z of EUV light source plasmas is required to achieve the target output.

1.2 Aim of this study

With this background, I have been involved in developing a collective LTS system because LTS has been recognized as a highly reliable method for measuring n_e and T_e based on experiences on measurement of nuclear fusion plasmas.[28]

In addition, the LTS which has high temporal and spatial resolution and can realize low disturbance is very useful for measuring the EUV light source plasma parameters.[29]

The significance of this paper is that establishment of a parameter measurement method of EUV light source plasmas without disturbance, and the state of the EUV light source plasmas was clarified for the first time.

1.3 Structure of this thesis

Chapter 1 introduces the EUV lithography, the background of this study and the composition of this doctoral thesis.

Chapter 2 indicates the principles of LTS and plasma production by laser. The theories of Rayleigh scattering and Thomson scattering were described in the first half. In the second half, the principle of plasma production by laser, cut-off density, and plasma heating mechanisms are described.

Chapter 3 describes the development of an ion feature measurement system and the results of the diagnostic of a EUV light source plasmas. The developed diagnostic system was applied to EUV light source plasmas. By changing the injection timing of the CO_2 laser, three different types of plasmas were generated. The CEs of the three types of plasmas differed, and ranged from 2.8 to 4.0%. Regarding the different plasma conditions, the spatial profiles of n_e, T_e, and Z were revealed and these results succeeded to explain the differences of the CEs.

In chapter 4, the ion feature and the electron feature of collective Thomson scattering of EUV light source plasmas were simultaneously detected for the first time. A purpose is to realize the measurement of n_e, T_e, T_i, and Z of the plasmas without any assumptions. Since the intensity of the electron feature is very weak compared to self-emissions from the plasma, efforts were concentrated to detect the peak wavelength of the electron feature.

By designing the spectrometer system appropriately and optimizing the scattering geometry, it was succeeded to detect the peak of the electron feature with the signal-to-noise ratio larger than one.

Chapter 5 summarizes the results obtained in this study and indicates future prospectives.

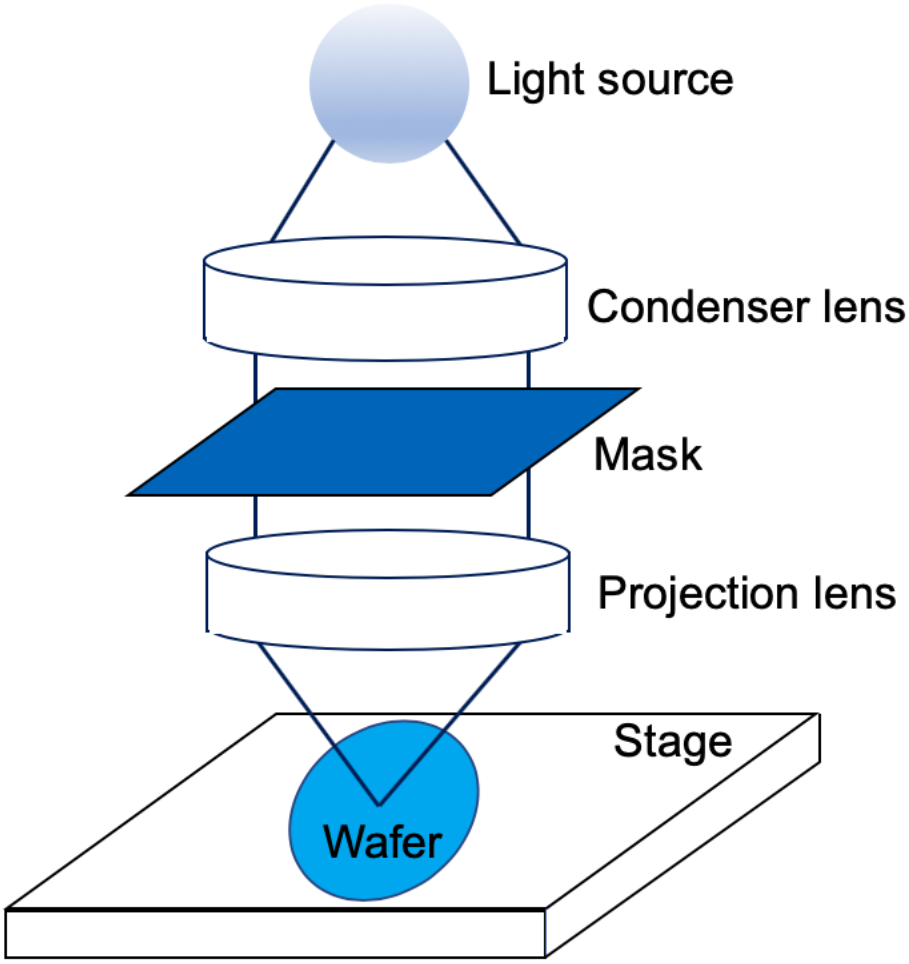

Fig. 1.1 Typical configuration of a lithographic apparatus

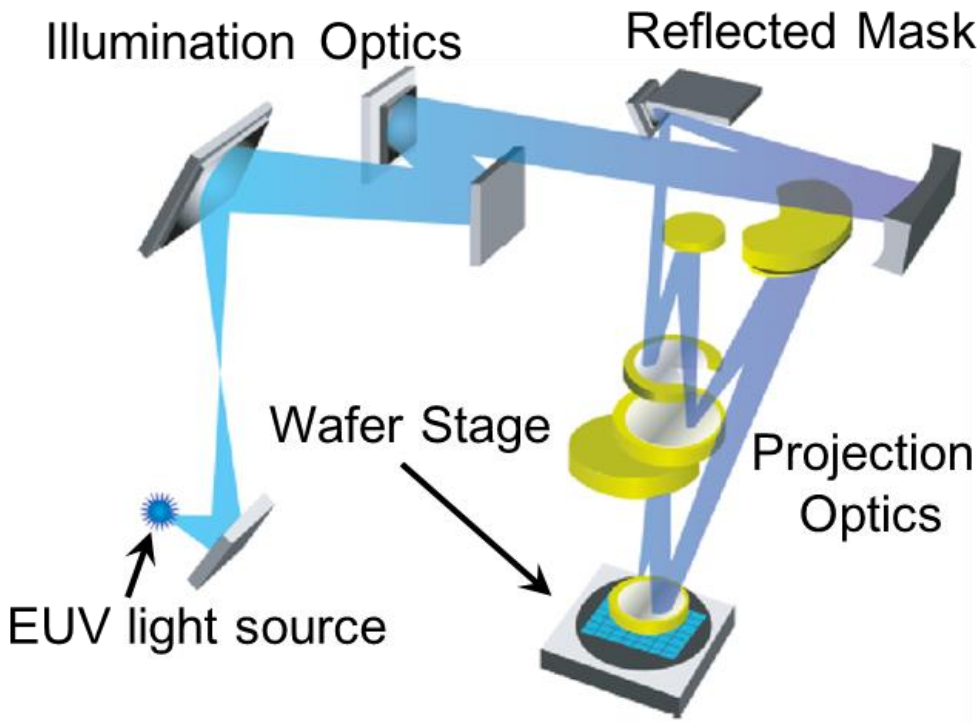

Fig. 1.2 Schematic diagram of EUV lithography

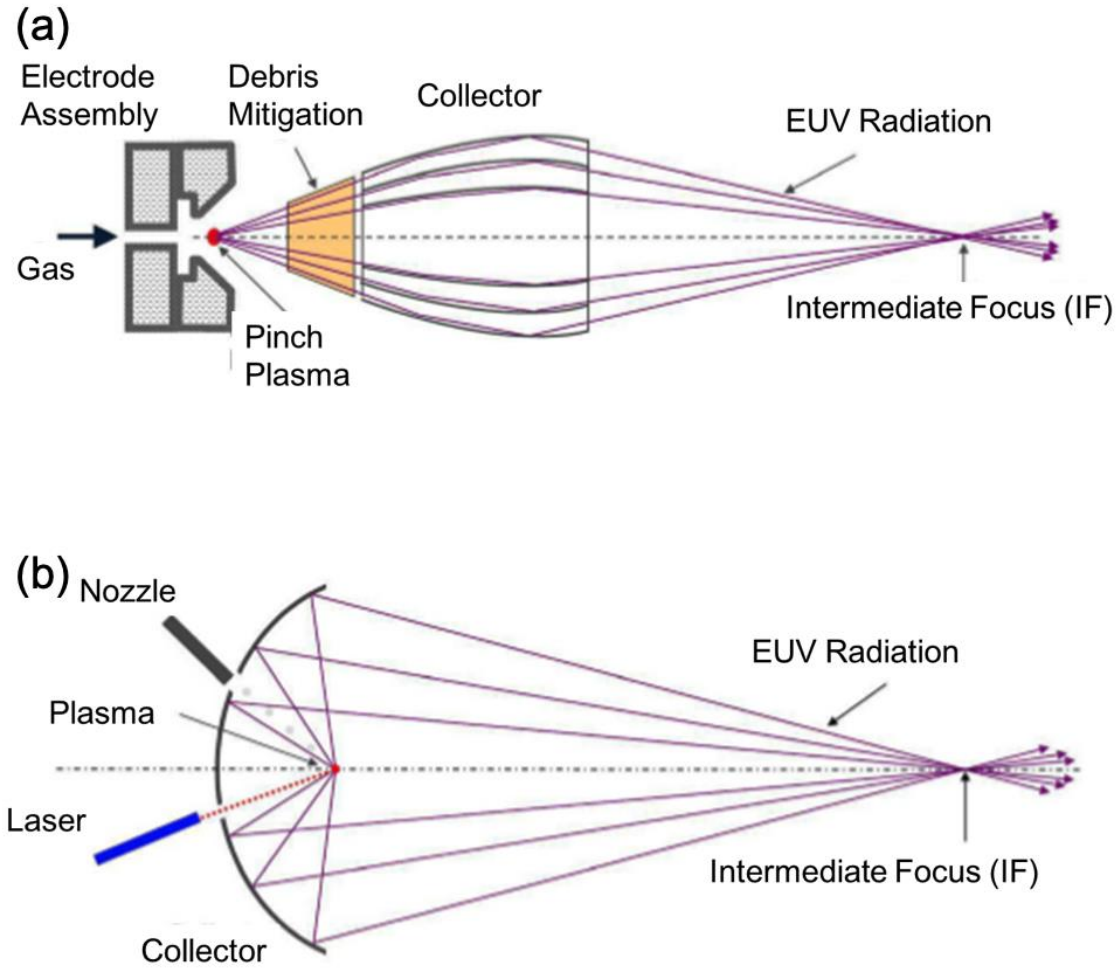

Fig. 1.3 Schematic diagrams of (a) DPP and (b) LPP[2]

References

[1] H. Kinoshita, K. Kurihara, Y. Ishii, and Y. Torii: J. Vac. Sci. & Technol., B7 1648 (1989)

[2] B. Wu and A. Kumar, Appl. Phys. Rev., vol. 1, no. 1, p. 011104, (2014).

[3] C. Wagner and N. Harned, Nat. Photonics 4, 24-26 (2010).

[4] Gerry O'Sullivan, Bowen Li, Rebekah D'Arcy, Padraig Dunne, Paddy Hayden, Deirdre Kilbane, Tom McCormack, Hayato Ohashi, Fergal O'Reilly, Paul Sheridan, Emma Sokell, Chihiro Suzuki and Takeshi Higashiguchi, J. Phys. B: At. Mol. Opt. Phys. 48, 144025 (2015).

[5] S. Inoue, T. Amano, T. Itani, H. Watanabe, I. Mori, T. Watanabe, H. Kinoshita, H. Miyai and M. Hatakeyama, Adv. Opt. Technol., 1, 269–278 (2012).

[6] A. M. Hawryluk and L. G. Seppala, J. Vac. Sci. Technol. B 6, 2162 (1988).

[7] J. E. Bjorkholm, J. Bokor, L. Eichner, R. R. Freeman et al., J. Vac. Sci. Technol. B 8, 1509 (1990).

[8] H.Fiedorowicz, A. Bartnik, Z. Patron, and P. Parys: Appl. Phys. Lett. 62, 2778 (1993).

[9] Bjorn Hansson, Hans M. Hertz: J. Phys. D: Appl. Phys. 37 3233 (2004).

[10] L. Rymell, L. Malmqvist, M. Berglund, and H. M. Hertz: Microelectronic Engineering 46 453 (1999).

[11] T. Mochizuki, Proc. SPIE, vol.3886, 306 (2000).

[12] N. R. Fornaciari, et. al, Proc. SPIE, vol.4343 226 (2001).

[13] W. N. Partlo, et. al. Proc. SPIE, vol.4343 232 (2001).

[14] B. A. M. Hansson and H. Hertz, J. Phys. D: Appl. Phys. 37, 3233 (2004).

[15] F. Massines, A. Rabehi, P. Decomps, R. B. Gadri, P. Segur and C. Mayoux, J. Appl. Phys., vol. 83, no. 6, p. 2950, (1998).

[16] R. Peeters, S. Lok, E. Alphen, N. Harned, P. Kuerz, M. Lowisch, H. Meijer, D. Ockwell, E. Setten, G. Schiffelers, J. W. Horst, J. Stoeldraijer, R. Kazinczi, R. Droste, H. Meiling, R. Kool, SPIE, 96791F, (2013).

[17] W. Svenden and G. O'Sullivan, *Phys. Rev. A,* vol. 50, p. 3710, (1994).

[18] G. O'Sullivan and R. Fraulkner, *Opt. Eng.,* vol. 33, p. 3978, (1994).

[19] J. R. Freeman, S. S. Harilal, and A. Hassanein, J. Appl. Phys., 110, 083303, (2011).

[20] S. Fujioka, M. Shimomura, Y. Shimada, S. Maeda, H. Sakaguchi, Y. Nakai, T. Aota, H. Nishimura, N. Ozaki, A. Sunahara, K. Nishihara, N. Miyanaga, Y. Izawa, and K. Mima, Appl. Phys. Lett. 92 (2008).

[21] H. Matsukuma, A. Sunahara, T. Yanagida, H. Tomuro, K. Kouge, T. Kodama, T. Hosoda, S. Fujioka, and H. Nishimura, Appl. Phys. Lett., 107, 121103 (2015)

[22] K. Nishihara, A. Sunahara, A. Sasaki, M. Nunami, H. Tanuma, S. Fujioka, Y. Shimada, K. Fujima, H. Furukawa, T. Kato, F. Koike, R. More, M. Murakami, T. Nishikawa, V. Zhakhovski, K. Gamata, A. Tanaka, H. Ueda, H. Nishimura, Y. Izawa, N. Miyanaga and K. Mima, Phys. Plasmas, 15, 056708, (2008).

[23] Y. Tao, H. Nishimura, S. Fujioka, A. Sunahara, M. Nakai, T. Okuno, N. Nishihara, N. Miyanaga and Y. Izawa, Appl. Phys. Lett., vol. 37, p. 201501, (2005).

[24] S. Katsuki, A. Kimura, Y. Kondo, H. Hotta, T. Namihira, T. Sakugawa and H. Akiyama, J. Appl. Phys., vol. 99, p. 013305, (2006).

[25] E. R. Kieft, J. J. A. M. ven der Mullen, G. M. W. Kroesen, V. Banine and K. N. Koshelev, Phys. Rev. E, vol. 70, p. 066402, (2004).

[26] E. R. Kieft, J. J. A. M. ven der Mullen, G. M. W. Krosen, V. Banine and K. N. Koshelev, Phys. Rev. E, vol. 70, p. 056413, (2004).

[27] E. R. Kieft, J. J. A. M. van der Mullen and V. Banine, Phys. Rev. E, vol. 72, p. 026415, (2005).

[28] N. Peacock, D. Robinson, M. J. Forrest, P. D. Wilcock and V. V. Sannikov, Nature, vol. 224, p. 488, (1968).

[29] K. Muraoka and A. Kono, J. Phys. D: Paal. Phys., vol. 44, p. 043001, (2011).

Chapter 2

Principles of plasma parameter measurement and plasma production

2.1 Introduction

2.1.1 Plasma parameter measurement

A method of investigating the conditions of plasmas by irradiating a laser beam to the plasmas is superior to the method of analyzing the radiation from the plasmas. This is because there is little ambiguity in the interpretation of the results. When the electromagnetic wave propagates through the plasma, its form can be classified into three, that is, transmission, refraction, and scattering. Among these, in the measurement of transmitted waves and refraction phenomena, information of the plasma density can be only obtained. In addition, the information is an integrated value along the optical path in the plasma, and no local value can be measured. On the other hand, in the measurement of scattering phenomena, it is possible to measure density and temperature as local values. The scattered wave is measured from a direction different from the incident wave and has information of the scattered light intensity, which depends on the electron density, and the scattered light spectrum affected by the condition of the plasma. Therefore, the laser scattering method is an extremely effective means for knowing the spatial structure of EUV light source plasmas.

2.1.2 Plasma production

Laser-produced plasmas (LPP) are used for the EUV light sources. When a material is irradiated with a laser, the surface of the irradiated material is ejected as gas or plasma. This is called laser ablation. In the laser ablation, the target material is often a solid or a liquid at the start of laser irradiation, and the state changes to gas or plasma by the irradiation of the high intensity laser. This chapter also briefly describes how the laser irradiated material changes into the plasma state, focusing on the generation of free electrons.

2.2 Laser diagnostic method[1][2]

Laser scattering method is outlined below. When the wavelength of the incident electromagnetic wave is λ_0 (nm) and the intensity is I_0 (W/m^2), as shown Fig. 1, the scattered light intensity I (θ,λ), whose wavelength is between λ and $\lambda+d\lambda$, in the θ (rad) direction at position r (m) is expressed as:

$$I(\lambda,\theta)d\Omega d\lambda \propto I_0 nV d\Omega d\lambda \tag{2.1}$$

Where, n (m^{-3}) is particle number density participating in scattering, V (m^3) is scattering volume. In the equation (2.1), the proportional constant is called the differential scattering cross section σ (λ, θ), and when this is applied to equation (2.1), it becomes equation (2.2).

$$\boldsymbol{I(\lambda,\theta)d\Omega d\lambda = I_0 nV\sigma(\lambda,\theta)d\Omega d\lambda} \qquad (\mathbf{2.2})$$

The value of σ (λ, θ) depends on the wavelength of electromagnetic waves, the type of scattering particles, and the state of the plasmas. The direction in which electrons are vibrated by electromagnetic waves depends on the electric field direction of electromagnetic waves.

The scattering is classified by the wavelength λ_0 of the incident electromagnetic wave and the type of particles scattered. When the particle is a neutral particle and its diameter is sufficiently smaller than the wavelength of the incident electromagnetic wave, it is called Rayleigh scattering. If its diameter is equal to or greater than the wavelength of the incident electromagnetic wave, it is called mie scattering. In this study, the main purpose is to measure the n_e, T_e, and Z of laser produced Sn plasmas produced for EUV light source, which has large temporal and spatial characteristic changes. Application of Thomson scattering method and absolute value calibration by Rayleigh scattering enables time-space resolved measurement of electron density and electron temperature of the plasmas. The principle of Rayleigh scattering and Thomson scattering are described below.

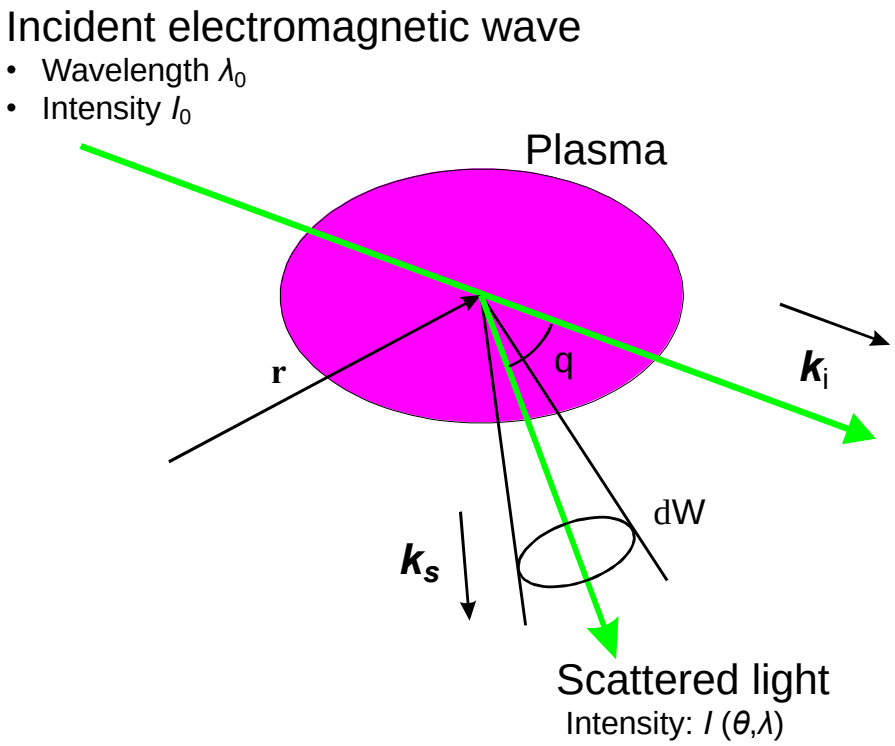

Fig. 2.1 Scattering of electromagnetic waves by plasma

2.2.1 Rayleigh scattering

Rayleigh scattering is electromagnetic wave emitted as a result of constrained electrons in the neutral particle being forcibly vibrated by the electric field of the incident electromagnetic wave. The characteristic of Rayleigh scattering is that the intensity of the scattered light is proportional to the pressure and not affected by the shape of particles. The derivation of scattering cross section of Rayleigh scattering is shown below briefly.

When the incident electromagnetic wave is a plane wave of monochromatic light, the electromagnetic wave induces an electric dipole moment in atoms or molecules, and dipole radiation occurs. If the size of the dipole is sufficiently small compared to the wavelength of the light, the magnitude of the electromagnetic field acting on the dipole is constant throughout the dipole. Therefore, the force acting on electrons can be expressed as:

$$E = E_0 \ exp^{j\omega t} \tag{2.3}$$

Where, E_0 is the magnitude of the electric field, ω is Angular frequency of incident electromagnetic wave. The equation of motion of electrons can be written as follows:

$$m\frac{d^2x}{dt^2} + m\omega_0^2 x = \ eE_0 exp^{j\omega t} \tag{2.4}$$

Where e is charge of electron, m is electron mass, and ω_0^2 is natural frequency. The first term on the left side shows the inertial force caused by electrons having mass. The second

term shows the force acting on bound electrons, and the binding force is proportional to the variation from the origin. The coefficient is $m\omega_0^2$ according to Hooke's law. Natural vibration does not interfere with forced vibration. When $x = x_0\, exp^{j\omega t}$ is substituted and the differential equation is solved, *x* becomes as follows:

$$x = \frac{eE_0}{m(\omega_0^2 - \omega^2)} exp^{j\omega t} \tag{2.5}$$

At this time, the dipole moment *M* is expressed by the following equation.

$$M = ex = \frac{e^2 E_0}{m(\omega_0^2 - \omega^2)} exp^{j\omega t} \tag{2.6}$$

When the incident light is polarized, the differential scattering cross section $\sigma_R(\theta)$ per unit solid angle is obtained. This is obtained from the ratio of the time average of the pointing vector of the energy radiated to the unit solid angle by the oscillating dipole of the moment *M* and the time average of the pointing vector of the incident plane wave, and is as follows.

$$\sigma_R(\theta) = r_0^2 \left(\frac{\omega^2}{\omega_0^2 - \omega^2}\right)^2 \left(\frac{1 + cos^2\,\theta}{2}\right) \tag{2.7}$$

Where θ is scattering angle, and r_o is classical electron radius and expressed as:

$$r_0 = \frac{e^2}{4\pi\varepsilon_0 m_e c^2} = 2.82 \times 10^{-15} \tag{2.8}$$

As described in the next page, since$\omega_0 \gg \omega$, ω in the denominator of (2.7) can be ignored.

$$\sigma_R(\theta) = r_0^2 \left(\frac{\omega}{\omega_0}\right)^4 \left(\frac{1 + cos^2\,\theta}{2}\right) \tag{2.9}$$

When the equation (2.9) is multiplied by 2π sin$\theta d\theta$ and integrated, the cross section of Rayleigh scattering can be written as:

$$\sigma_R = \frac{8\pi}{3} r_0^2 \left(\frac{\omega}{\omega_0}\right)^4 \tag{2.10}$$

This equation shows that the light scattering is inversely proportional to the fourth power of the wavelength and is called the Rayleigh scattering equation. The Rayleigh signal is a signal from neutral particles, and information on neutral particles is obtained by measuring Rayleigh scattering. Also, using the property that the scattered light intensity of Rayleigh scattering is proportional to the number of particles, it is possible to calibrate the absolute value of the light receiving optical system.

The cross section for Rayleigh scattering depends on the species, which means that the measurement should be done with the same gas composition. For instance, the cross section of argon, nitrogen, and oxygen are 5.4×10^{-32} m^2, 6.2×10^{-32} m^2, and 5.3×10^{-32} m^2, respectively.[3][4][5]

2.2.2 Thomson scattering

When an electromagnetic wave is injected to a stationary electron, the electron is accelerated by the electric field and radiates an electromagnetic wave having the same frequency as the incident electromagnetic wave. Scattering of electromagnetic waves by this free electron is called Thomson scattering. When laser light enters isotropic plasma and is scattered by electrons in plasma, the scattered light intensity is not multiplied by the number of electrons of scattered light intensity by one electron. This is because the electron density is not completely uniformly distributed spatially due to thermal fluctuation or the like. That is, scattered waves are not completely canceled, and observation is possible. Since the theory of Thomson scattering has already been established, it will be briefly described within the range where the relational expression necessary for the scattering measurement is clarified.

In the coordinate system shown in Fig. 2.2, when a plane monochromatic electromagnetic wave $\boldsymbol{E}_{\mathrm{i}}$ enters one electron at position $\boldsymbol{r}_{\mathrm{l}}$, electrons are accelerated and emit electromagnetic waves. $\boldsymbol{E}_{\mathrm{i}}$ is expressed as:

$$\boldsymbol{E}_i = \boldsymbol{E}_0 \exp[j\ \{\boldsymbol{k}_0 \cdot \boldsymbol{r}_l(t) - \omega_0 t\}] \tag{2.11}$$

Where, $\boldsymbol{k}_{\mathrm{o}}$ is wave number vector, ω_0 is angular frequency, $\boldsymbol{E}_0$ is Electric field strength vector. And then, the acceleration of the electron is:

$$\frac{d^2\boldsymbol{r}_l}{dt^2} = -\frac{e}{m}\boldsymbol{E}_0 \exp[j\{\boldsymbol{k}_0 \cdot \boldsymbol{r}_l(t) - \omega_0 t\}] \tag{2.12}$$

Where, e is elementary charge, m is mass of an electron. The electromagnetic field of the scattered wave at the detector position $\boldsymbol{R}$ in the wave belt can be written as follows:

$$\begin{aligned}\boldsymbol{B}(\boldsymbol{R},t) &= -\frac{\mu_0 e}{4\pi R}(\boldsymbol{\nabla}_R t')\frac{d^2\boldsymbol{r}(t')}{dt^2} \\ &\approx -\frac{\mu_0 e^2}{4\pi m c^2}\left(\frac{\boldsymbol{R}\times\boldsymbol{E}_0}{R^2}\right) exp\left[j\left\{\boldsymbol{k}\cdot\boldsymbol{r}_l\left(t-\frac{R}{c}\right)-\omega_0\left(t-\frac{R}{c}\right)\right\}\right]\end{aligned} \tag{2.13}$$

$$\boldsymbol{E}(\boldsymbol{R},t) \approx \ -\frac{e^2}{4\pi\varepsilon_0 m c^2}\left(\frac{(\boldsymbol{R}\times\boldsymbol{E}_0)\times\boldsymbol{R}}{R^3}\right) exp\left[j\left\{\boldsymbol{k}\cdot\boldsymbol{r}_l\left(t-\frac{R}{c}\right)-\omega_0\left(t-\frac{R}{c}\right)\right\}\right] \tag{2.14}$$

Where, μ_0 and ε_0 are permeability and dielectric constant in vacuum, respectively, c is speed of light, $R = |\mathbf{R}|$. A delay time t' is as:

$$t' = t - \frac{|\boldsymbol{R}-\boldsymbol{r}(t')|}{c} \approx t - \frac{R}{c} + \frac{\left\{\boldsymbol{R}\cdot\boldsymbol{r}\left(t-\frac{R}{c}\right)\right\}}{Rc} \tag{2.15}$$

Also, $\boldsymbol{k} = \boldsymbol{k}_0 - (\omega_0/c)(\boldsymbol{R}/R)$, $(\omega_0/c)(\boldsymbol{R}/R)$ is a wave vector of a scattered wave ($\boldsymbol{k}_s = (\omega_0/c)(\boldsymbol{R}/R)$). Since scattering of visible light is considered here, the transition of momentum to electrons can be neglected. Therefore, the magnitude of k is expressed as follows using scattering angle θ_s.

$$k \equiv |\boldsymbol{k}| = 2\frac{\omega_0}{c} sin\left(\frac{\theta_s}{2}\right) \tag{2.16}$$

The electromagnetic field of scattered waves due to N electrons is the sum of l in Eq. (2.13) and Eq. (2.14) and can be expressed as follows.

$$E_s(\boldsymbol{R}, t) \approx -\frac{e^2}{4\pi\varepsilon_0 mc^2}\left(\frac{(\boldsymbol{R} \times \boldsymbol{E}_0) \times \boldsymbol{R}}{R^3}\right) \sum_{l}^{N} exp\left[j\left\{\boldsymbol{k}\boldsymbol{r}_l\left(t - \frac{R}{c}\right) - \omega_0\left(t - \frac{R}{c}\right)\right\}\right] \tag{2.17}$$

$$\boldsymbol{B}_s(\boldsymbol{R}, t) = \left(\frac{\boldsymbol{R} \times \boldsymbol{E}_s}{cR}\right) \tag{2.18}$$

From Eq. (2.17) and (2.18), the pointing vector is:

$$S_p(\boldsymbol{R}, t) = \frac{1}{\mu_0}(E_s \times B_s) = c\varepsilon_0 |E_s|^2 \frac{\boldsymbol{R}}{R} \tag{2.19}$$

The average power reaching the detector is given by Eq. (2, -).

$$\langle \boldsymbol{S}_p \rangle d\boldsymbol{s} = \left|\langle \boldsymbol{S}_p \rangle\right| \boldsymbol{R}^2 d\Omega \tag{2.20}$$

Where, d$\boldsymbol{s}$ is a surface-element vector of a detector, $d\Omega$ is the solid angle to be stretched by the detector, the symbol $\langle\ \rangle$ is a time average which is sufficiently longer than the period of electromagnetic waves or a transparent ensemble average.

What should be derived here is the frequency distribution of the scattering power reaching the detector. According to the theorem of A, the frequency distribution can be expressed as follows using the autocorrelation function Fourier transform of the field variables.

$$I(\boldsymbol{k},\omega)=\frac{1}{2\pi}\int_{-\infty}^{\infty}d\tau e^{-j\omega\tau}c\varepsilon_0\langle \boldsymbol{E}_s(\boldsymbol{R},t)\cdot\boldsymbol{E}_s^*(\boldsymbol{R},t+\tau)\rangle \tag{2.21}$$

By substituting Equations 2 and 3 into Equation 1, the differential scattering cross section is defined by the following equation:

$$I(\boldsymbol{k},\omega)d\omega R^2 d\Omega=\mathrm{N}I_0\sigma(\boldsymbol{k},\omega)d\omega d\Omega \tag{2.22}$$

Where, I_0 (= $c\varepsilon_0|E_0|^2$) is incident wave intensity. Then, $\sigma(\boldsymbol{k},\omega)$can be written as follows:

$$\begin{aligned}\sigma(\boldsymbol{k},\omega)=&\left\{\left(\frac{e^2}{4\pi\varepsilon_0 mc^2}\right)^2\left(\frac{(R\times E_0)\times R}{R^3}\right)^2\right\}\\&\times\frac{1}{2\pi N}\int_{-\infty}^{\infty}d\tau e^{-j\omega\tau}\left\langle\sum_{l,m}^{N}e^{j\{\boldsymbol{k}\cdot\boldsymbol{r}_l(t)-\omega_0 t\}}\cdot e^{-j\{\boldsymbol{k}\cdot\boldsymbol{r}_l(t+\tau)-\omega_0(t+\tau)\}}\right\rangle\\=&\sigma_T(\varphi)S(\boldsymbol{k},\omega)\end{aligned} \tag{2.23}$$

The dynamic form factor$S(\boldsymbol{k},\omega)$, which is important in considering the actual spectrum, is expressed as:

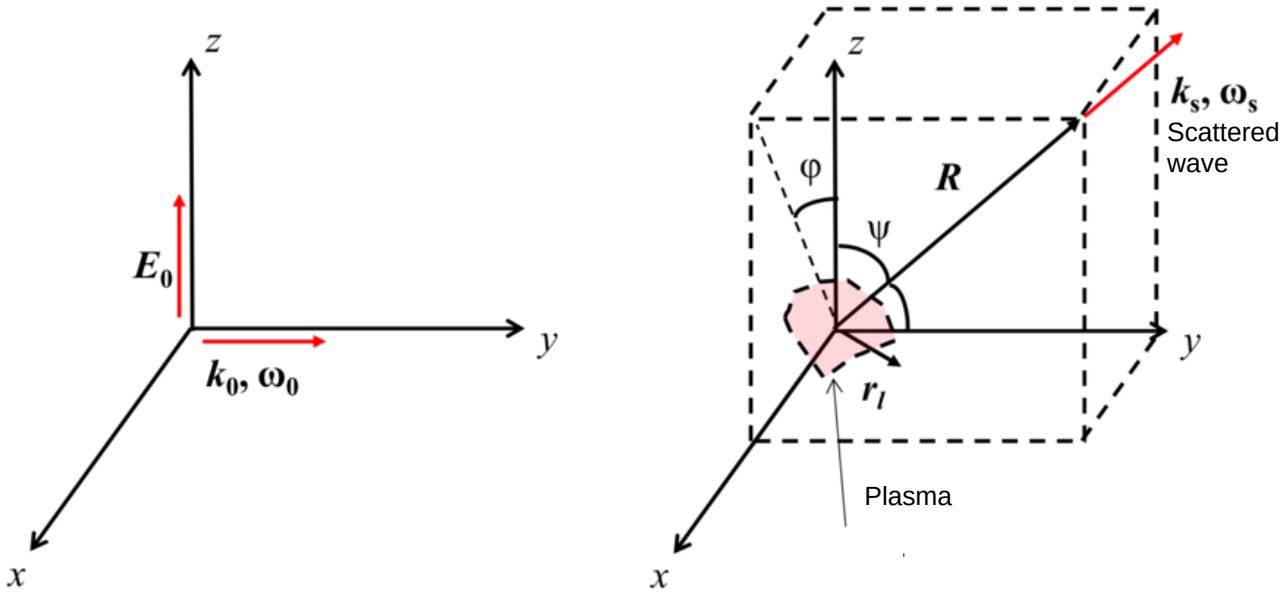

Fig. 2.2 Coordinate system of laser scattering

$$S(\boldsymbol{k},\omega) = \frac{1}{2\pi N}\int_{-\infty}^{\infty} d\tau e^{-j\omega\tau}\left\langle \sum_{l,m}^{N} e^{j\{\boldsymbol{k}\cdot\boldsymbol{r}_l(t)-\omega_0 t\}} \cdot e^{-j\{\boldsymbol{k}\cdot\boldsymbol{r}_l(t+\tau)-\omega_0(t+\tau)\}}\right\rangle$$

$$= \frac{1}{2\pi N}\int_{-\infty}^{\infty} d\tau e^{-j(\omega-\omega_0)\tau}\left\langle \sum_{l,m}^{N} e^{j\{\boldsymbol{k}\cdot\boldsymbol{r}_l(t)\}} \cdot e^{-j\{\boldsymbol{k}\cdot\boldsymbol{r}_l(t+\tau)\}}\right\rangle$$

$$= \frac{1}{2\pi N}\int_{-\infty}^{\infty} d\tau e^{-j(\omega-\omega_0)\tau}\langle n_e(\boldsymbol{k},t) n_e^*(\boldsymbol{k},t+\tau\rangle \qquad (2.24)$$

The difference angle frequency is defined as $\Delta\omega = \omega - \omega_0$, and in the following the dynamic form factor is denoted by$S(\boldsymbol{k},\Delta\omega)$. As shown in Eq. (2, 24), the scattered light spectrum is obtained by taking the spatial Fourier component of the electron density fluctuation having the same wave number vector as the wave vector k determined by the shape of the scattering system and Fourier transforming the autocorrelation function with respect to time. In order to calculate the scattered light spectrum, it is a problem to obtain the spectrum of oscillation of the electron density in the plasma. The electrons and ions in the plasma are related to each other by Coulomb interaction. This influence extends to the extent of Debye length λ_D of electrons. Wavelength of oscillation of electron density and λ_D are important for determining the scattering spectrum, and parameter $\alpha \equiv 1/(k\lambda_D)$ was introduced.[6] Consider an isotropic collision less plasma consisting of electrons and one kind of ions. When the electron and ion temperatures have Maxwellian distribution, the dynamic form factor is expressed by the following equation using the Salpeter approximation.[7]

$$S(\boldsymbol{k},\omega)d(\Delta\omega) = \frac{1}{\pi^{\frac{1}{2}}}\Gamma_{\alpha}(x_e)dx_e + \frac{1}{\pi^{\frac{1}{2}}}Z\left(\frac{\alpha^2}{1+\alpha^2}\right)\Gamma_{\beta}(x_i)dx_i \qquad (2.25)$$

Where, κ is Boltzmann constant.

$$\Gamma_{\gamma}(x) = \frac{\exp(-x^2)}{\left(1+\gamma^2-\gamma^2 g(x)\right)^2 + \pi\gamma^4 x^2 \exp(-2x^2)}$$

$$\mathrm{g(x)} = 2\mathrm{x}\exp(-\mathrm{x}^2)\int_0^x \exp t^2\, dt$$

$$\mathrm{x_e} = \frac{c\Delta\lambda}{2\lambda_i \sin\left(\frac{\theta}{2}\right)}\left(\frac{m}{2eT_e}\right)^{\frac{1}{2}}$$

$$\mathrm{x_i} = \frac{c\Delta\lambda}{2\lambda \sin\left(\frac{\theta}{2}\right)}\left(\frac{M}{2eT_i}\right)^{\frac{1}{2}}$$

$$\alpha = \frac{\lambda_{\mathrm{i}}}{4\pi \sin\left(\frac{\theta}{2}\right)}\left(\frac{n_e e^2}{\varepsilon_0 \kappa T_e}\right)^{\frac{1}{2}}$$

$$\beta = \left(\mathrm{Z}\frac{\mathrm{T_e}}{T_i}\frac{\alpha^2}{1+\alpha^2}\right)^{\frac{1}{2}}$$

The frequency spread of the first term of equation (2.25) is about Doppler broadening $k(2kT_e/m)^{1/2}$ due to the thermal velocity of electrons, which is called an electron feature. On the other hand, the frequency spread in the second term is about the Doppler spread S due to the thermal velocity of the ion, and is called an ion feature. Figure 2.3 shows the function which determines the spectra of these features.

The dynamic form factor, the ion feature and the electron feature are integrated with respect to the angular frequency and are denoted by S(k), S_e(k), and S_i(k), they are expressed as follows:

$$S(k) = S_e(k) + S_i(k) \tag{2.26}$$

$$S_e(k) = \frac{1}{1+\alpha^2} \tag{2.27}$$

$$S_i(k) = \frac{\mathrm{Z}\alpha^4}{(1+\alpha^2)\{1+a^2(1+ZT_e/T_i)\}} \tag{2.28}$$

Figure 2.4 shows α dependence of dynamic form factor under some conditions.[8]

The electron density is directly proportional to the intensity of the scattered light and can be obtained by integrating the intensity of the spectrum. Therefore, absolute sensitivity calibration of the scattered light detection system is required. This calibration can be easily performed by measuring Rayleigh scattering from a gas of known density. The spectral widths of the measured spectra are actually convolutions of the true scattered spectra (Thomson or Rayleigh) and the instrument function of the spectrometer used to measure the spectra.[9] In this study, the electron density is obtained from the scattered light intensity of the ion feature.

Using the Rayleigh scattering intensity I_R from the gas with known density n_N and scattering angle σ_R measured with the same optical system as Thomson scattering, the electron density can be written as:

$$n_e = n_N \frac{I_{th}}{I_R} \frac{\sigma_R}{\sigma_{th}} \frac{1}{S_i(k)} \tag{2.29}$$

Where I_{th} is total Thomson scattering intensity, σ_{th} is cross section of scattering of Thomson scattering.

In the above description, it is assumed that the charge of ions in the plasma is one type. However, if the plasma contains ions of different ionization stages and the difference between their mass and temperature can be neglected, the ion valence number can be replaced by averaged ionic charge defined as follows.

$$\bar{Z} = \frac{\sum_{l=1} n_l Z_l^2}{\sum_{l=1} n_l Z_l} \tag{2.30}$$

Where, n_{i} and Z_{i} are the density and ionic charge of one type of ion, respectively.

2.2.3 Scattering parameter α

The spectrum and intensity of Thomson scattered light have different properties in the case of $\alpha \ll 1$ and the case of $\alpha \geq 1$, as shown in section 2.2.2. When $\alpha \ll 1$, most of the scattered light intensity concentrates on the electron feature, and its spectrum reflects the electron velocity distribution function. This scattering is made by free electrons that move individually, which is called incoherent Thomson scattering.

On the other hand, in the case of $\alpha \geq 1$, collective effects of electrons and ions appear in scattering, which is called collective Thomson scattering. Figure 2.5 shows a collective

Thomson scattering spectrum, ion feature spectrum, electron feature spectrum, and whole spectrum (n_e = 4 × 10^{24} m^{-3}, T_e = T_i= 30 eV, Z=10, θ = 135°, and λ_i = 532 nm). The scattering spectrum consists of a central peak with strong intensity and symmetrical peaks on both sides of the center peak. The peak at the center is the ion feature and the side peak is the electron feature. It can be seen that the spectral width of the ion feature is narrower than the electron feature.

In both spectra, since the wavelength of the probing laser is at the center, it is easier to measure electron feature from the viewpoint of rejecting stray light and wavelength separation. However, in the EUV light source plasmas with high electron density, detection of the whole electron feature is difficult due to the influence of self-emission of the plasma.

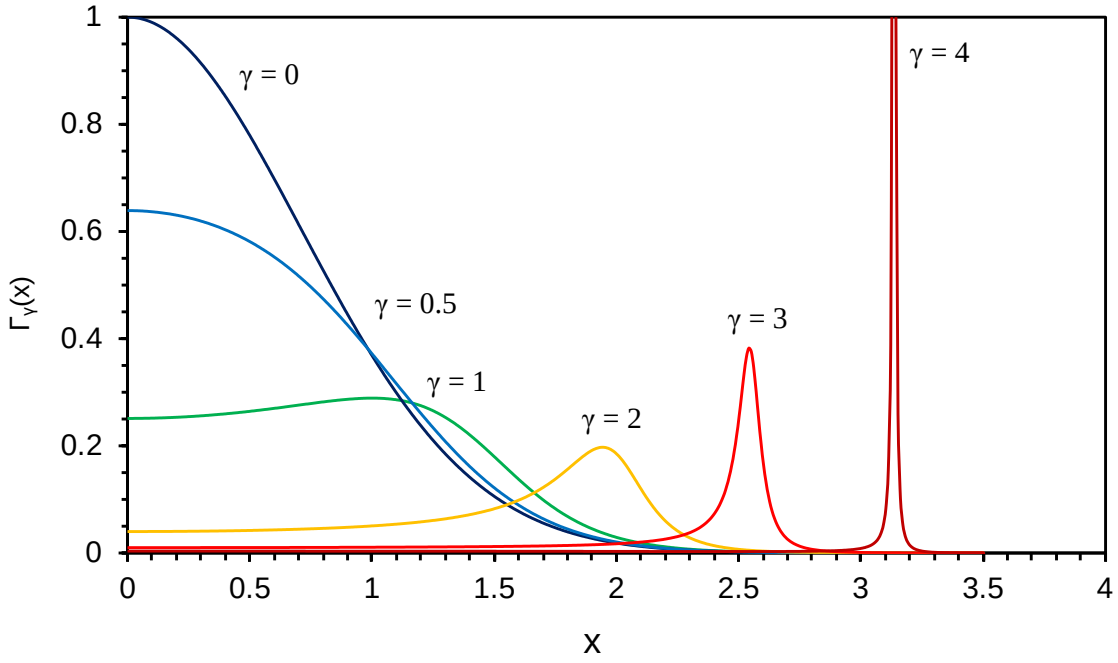

Fig. 2.3 Function of $\Gamma_\gamma(x)$

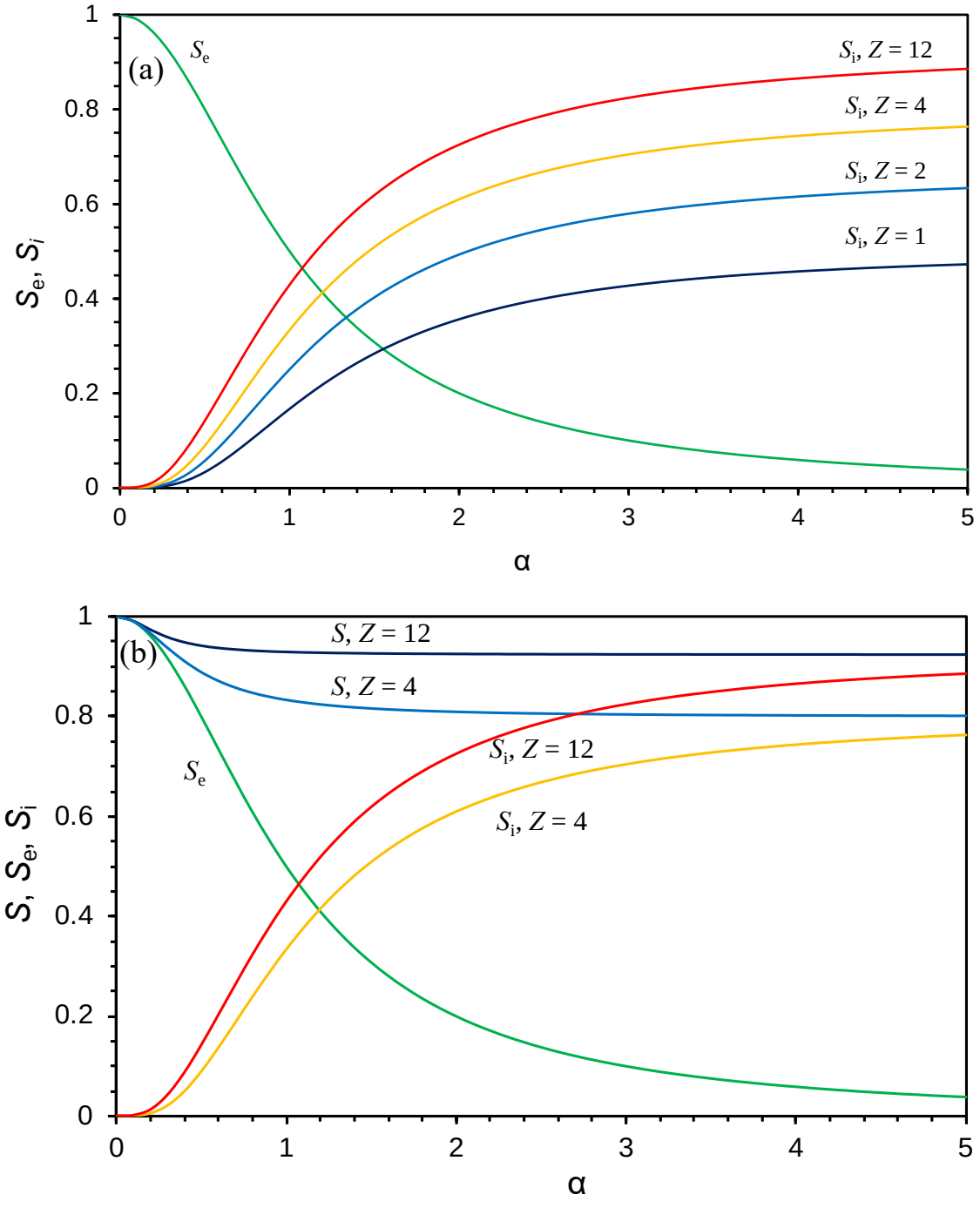

Fig. 2.4 (a) α dependence of S_e and S_i at $T_e = T_i$,
(b) α dependence of $S(=S_e + S_i)$, S_e and S_i at $T_e = T_i$, Z=4, 12

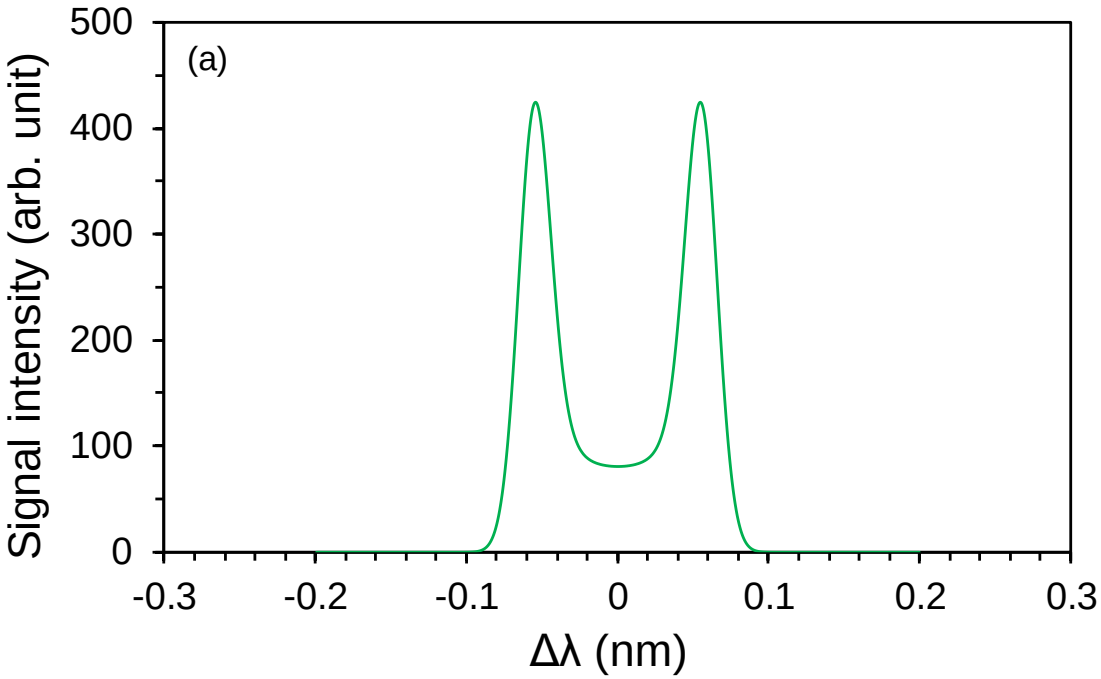
(a)
Signal intensity (arb. unit)
500
400
300
200
100
0
-0.3
-0.2
-0.1
0
0.1
0.2
0.3
Δλ (nm)

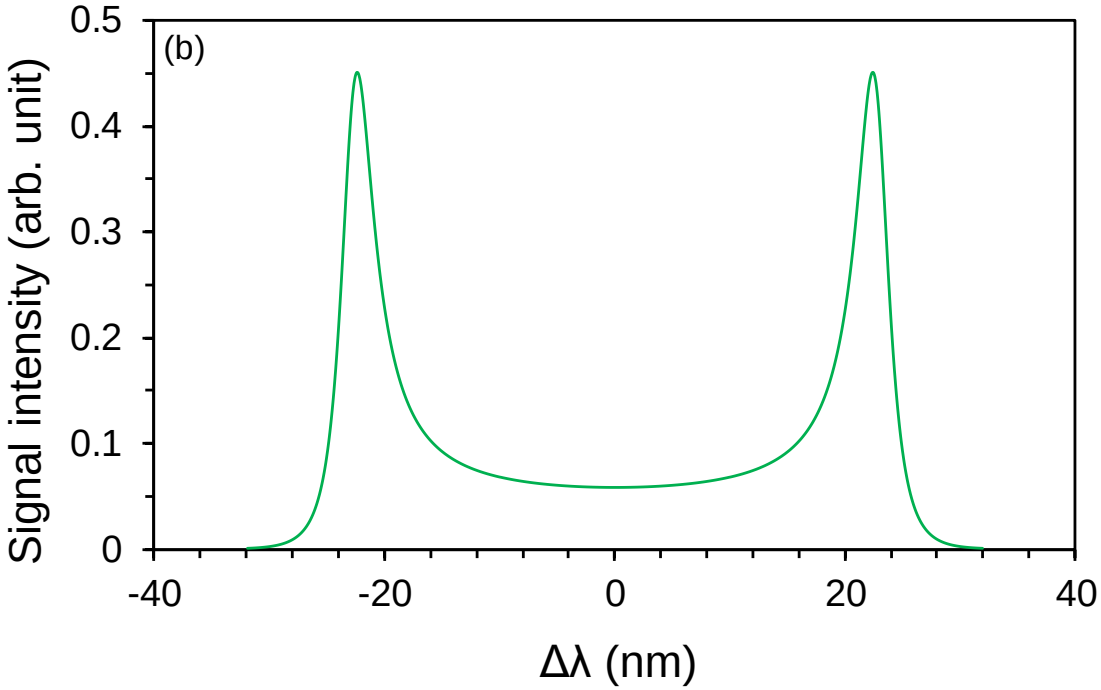
(b)
Signal intensity (arb. unit)
0.5
0.4
0.3
0.2
0.1
0
-40
-20
0
20
40
Δλ (nm)

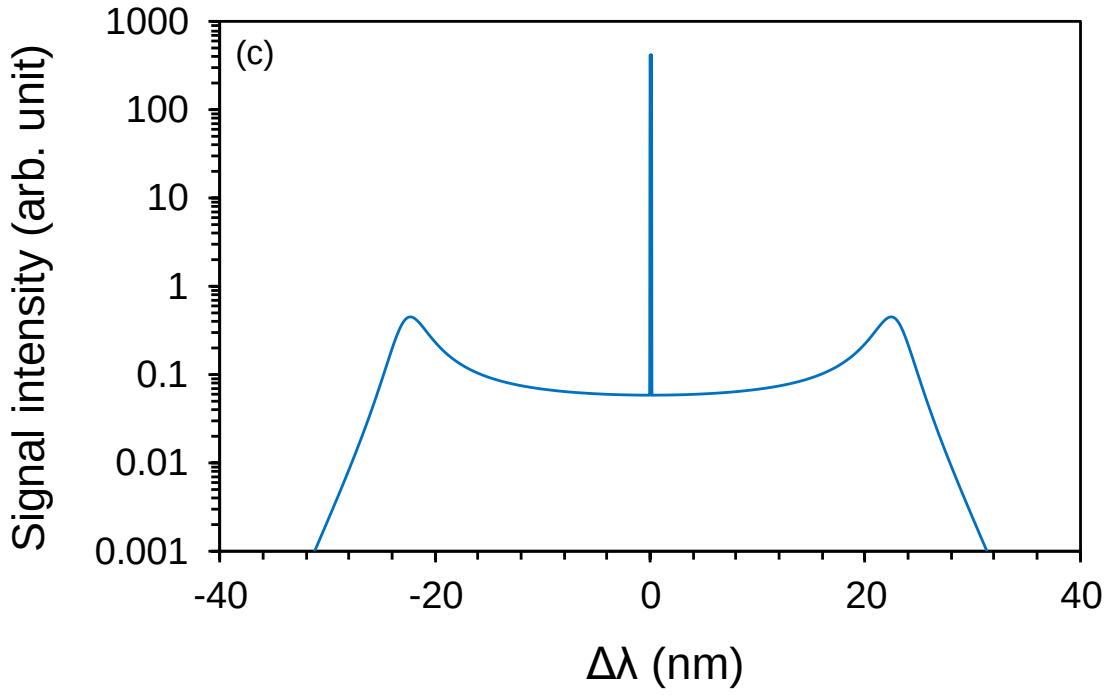

Fig. 2.5 (a) ion feature spectrum, (b) electron feature spectrum, and (c) whole spectrum of collective Thomson scattering. (n_e = 4 × 10^{24} m^{-3}, T_e = T_i= 30 eV, Z=10, θ = 135°, and λ_i = 532 nm)

2.3 Plasma production by laser[10][11]

2.3.1 Characteristics of laser-produced plasma

Low pressure gas is easily converted to plasma by applying radio frequency (RF) wave or microwave, but natural light which is the same electromagnetic wave, it is difficult to convert gas to plasma even if the intensity is the same. The difference between the two is that RF waves are coherent waves with uniform phases, whereas natural light is noncoherent waves. On the other hand, the laser was able to generate coherent light with very high brightness, and plasma generation by light became possible. LPP have different characteristics from the plasmas generated by direct current discharge and high frequency discharge. Here, representative seven characteristics of LPP is introduced.

1. Easily create high temperature / high density plasma.
2. High purity plasma can be obtained in a state of being completely separated from a vacuum container or the like.
3. Gas, liquid and solid can be converted into plasma.
4. Multivalent ion plasma can be easily produced.
5. A plasma having a very high pressure can be generated. In particular, when using implosion method it is more than the center of the sun.
6. A plasma which emits X-rays is obtained.
7. Very small (10 μm ~) plasma can be produced. However, plasma of large volume cannot be generated.

Various applied research utilizing these features exists. Main examples are nuclear fusion by laser, X-ray laser, biological observation, metal surface modification, elemental analysis by plasma spectroscopy and ultrafine particle generation and more. EUV light source plasma also uses these features.

2.3.2 Plasma production and cut-off density

The principle of plasma generation by laser can be understood by knowing the dielectric breakdown mechanism of gas which occurs when laser is focused on gas. In high-frequency discharge, an initial electron is accelerated by the high-frequency, and electron multiplication proceeds by the collision of electrons and atoms, resulting in dielectric breakdown. Discharge by laser also occurs in almost the same process. The difference is that the initial electron for electron multiplication are generated by multi-photon absorption process. Ionization in that case depends on laser intensity, but it is often caused by multiphoton absorption.[12] The ionization energy of Sn is 7.34 eV and the photon energies of CO_2 laser, which is used for EUV light source, (10.6 μm) and Nd: YAG laser, which was used in chapter 4, (1064 nm) are 0.12 eV and 1.17 eV, respectively. Considering the case of a CO_2 laser, 62 photons are simultaneously absorbed by Sn, and only one photoelectron is generated.

When the laser is incident on the solid or liquid target, the target is heated and vaporization occurs. Initial electrons are generated from the vaporized target and the generated electrons are heated by the inverse-bremsstrahlung process. In other words, electrons are vibrated by the laser and absorb laser energy by three-body collision of photons, atoms and electrons. The electrons that obtained energy collide with atoms, and

the number of electrons increases due to electron impact ionization. At that time, if more laser energy absorption than used for excitation and ionization, electron impact ionization occurs continuously and ionization progresses like an avalanche. This is called an avalanche. As a result, the number of free electrons is rapidly increased, and an initial plasma is generated. Then, plasma is produced by laser and plasma heating occurs.

When the laser is injected to the target, the laser is reflected at the critical density point. The electron density at critical density point is called the cut-off density n_c and is expressed by the following equation.

$$n_c = \frac{4\pi^2 m_e}{\mu_0 e^2 \lambda^2} \tag{2.31}$$

Where m_e is mass of electron, μ_0 is vacuum permeability, e is elementary charge, λ is wavelength of incident laser. Equation 2.31 can be obtained from the electron plasma frequency ω_{pe} which is expressed as $\omega_{pe} = \sqrt{e^2 n_e / \varepsilon_0 m_e}$. In this study, CO_2 laser (10.6 μm) and Nd: YAG laser (1064 nm) were used to generate the laser plasmas and the cut-off densities of the lasers were calculated to be 10^{25} m^{-3} and 10^{27} m^{-3}, respectively.

2.3.3 Plasma heating

When laser is irradiated on metal, laser propagates only to cut-off density. The problem of laser light absorption is important in laser plasma applications, because in EUV light sources, laser energy is absorbed by plasma and extracted as EUV light. Since high

conversion efficiency from laser to EUV light is required, it is indispensable that the laser absorption rate is sufficiently high.

Ionization proceeds as the electron temperature rises, and the generated plasma becomes a multiply ionized plasma of high temperature. The electron temperature of the generated plasma rises, the valence increases, and it becomes high temperature multiply ionized plasma. Energy is absorbed by inverse-bremsstrahlung process. The absorption coefficient K_a in this process can be written as follows:

$$K_a = \frac{Z^2 e^6 n_e n_i \ln\Lambda}{3\omega^2 c\varepsilon_0^2 (2\pi m_e k T_e)^{\frac{3}{2}} \left[1 - \left(\frac{\omega_{pe}}{\omega}\right)^2\right]^{\frac{1}{2}}} \tag{2.32}$$

Where $\ln\Lambda$ is coulomb logarithm. Laser energy is mainly absorbed in the high collision frequency region in the vicinity of the cut-off density. The unabsorbed laser is reflected at the critical density point of $n_e = n_c$. Here, one-dimensional plasma is considered and the distribution of electron density of LPP is assumed $n_e = n_c$ (1-x / L). Where L is scale length of electron density. As the laser enters the target from the vacuum side and propagates, the laser absorption increases with increasing plasma density. When the laser light reaches the critical density, it is reflected, bounced back to the vacuum side, and returns to the vacuum side while giving energy to the plasma again. The absorption rate can be written as follows:

$$\eta_a = 1 - \exp\left(-\frac{32}{15}\frac{\nu_{eic}}{c}L\right) \tag{2.33}$$

Where ν_{eic} is collision frequency of electrons and ions at critical density point. Since ν_{eic} is proportional to $T_e^{-3/2}$, the absorption coefficient decreases as the temperature rises. Calculating the energy injection from the laser to the plasma and the loss due to the heat conduction of the electrons gives the relationship between the laser intensity and the absorption rate η_a is expressed as:

$$\eta_a \ \ln(1-\eta_a)^{-1} = 10^{11}\frac{L\omega}{cI} \tag{2.34}$$

Where I is laser intensity and can be expressed as:

$$I = \varepsilon_0 cE^2 \tag{2.35}$$

Where ε_0 is vacuum dielectric constant, c is light speed, E is electric field strength of the light. Figure 2.5 shows a laser intensity dependence of absorptivity. As the laser intensity increases, the absorptance due to the inverse-bremsstrahlung decreases.

Figure 2.6 shows a scale length of electron density dependence of absorptivity of CO_2 laser and Nd: YAG laser when I is constant (= 5×10^{13} W/cm^2). Compared with Nd: YAG, it can be seen that CO_2 laser has extremely low absorption rate of laser. This is because the cut-off density is two orders of magnitude smaller than Nd: YAG. Therefore, if it is attempted to obtain sufficient laser absorption with a CO_2 laser, there is no choice but to increase the scale length.[12] Assuming one-dimensional isothermal expansion, the scale length L is determined by the product of sound speed and expansion time, and increasing the laser pulse width increases the L. That is, it is considered that the laser absorption rate

tends to increase with the long pulse. However, in actual practice, even if the laser pulse width is increased in the long pulse, the scale length does not easily increase. Since the EUV light source employs a CO_2 laser as the drive laser, in order to increase the absorption rate, before the CO_2 laser is irradiated, the scale length of the Sn droplet target is lengthened by another laser.[13]

In the laser Thomson scattering measurement, the increase in energy of the probing laser amplifies the Thomson scattering signal and improves the signal-to-noise ratio. However, if the energy is increased too much, disturbance of the plasma due to the probing laser becomes problem. In order to measure the EUV light source plasma with sufficient spatial resolution, it is necessary to set the laser spot size to about 50 μm. Then, as the laser power density increases, there is concern that the electron temperature will rise due to the inverse-bremsstrahlung process. The influence is formulated as follows, and it becomes a problem in plasma with high electron density and low electron temperature.[14]

$$\frac{\Delta T_e}{T_e} = 5.32 \times 10^{-11} \left(\frac{n_e Z}{T_e^{3/2}}\right) \lambda^3 \left\{1 - exp\left(-\frac{h\nu}{eT_e}\right)\right\} I_0 \Delta\tau \qquad (2.35)$$

Where n_e is electron density (m^{-3}), T_e is electron temperature (eV), λ is laser wavelength (m), h is Planck constant (J·s), ν is frequency of laser photon (Hz), I_o is laser power density (W/m2), $\Delta\tau$ is laser pulse width (s).

In this equation, it is assumed that the energy absorbed by the inverse-bremsstrahlung process in the laser spot is directly converted to the thermal energy of the electrons.

However, if the thermal diffusion coefficient χ $[=\kappa/(5/2n_e k_B)]$ of the plasma is sufficiently large, the absorbed energy is also distributed to electrons that are away from the laser spot radius r_0 by Δr [= $(\chi\Delta\tau)^{1/2}$]. Where κ is heat conduction coefficient of Spitzer[15], k_B is Boltzmann constant. That is, due to thermal diffusion, the rise rate of the electron temperature is the product of the value $\Delta T_e/T_e$ calculated by Eq. 2.35 and $(r_0/(r_0+\Delta r))^2$.

2.4 Summary

This chapter described the principles of laser diagnostic method and plasma production by laser. Rayleigh scattering and Thomson scattering were indicated in the first half.

In the second half, the principle of plasma production by laser, the cut-off density, and the plasma heating mechanism were described. Plasma heating due to the probing laser which is important factor when applying Thomson scattering to EUV light source plasmas was mentioned.

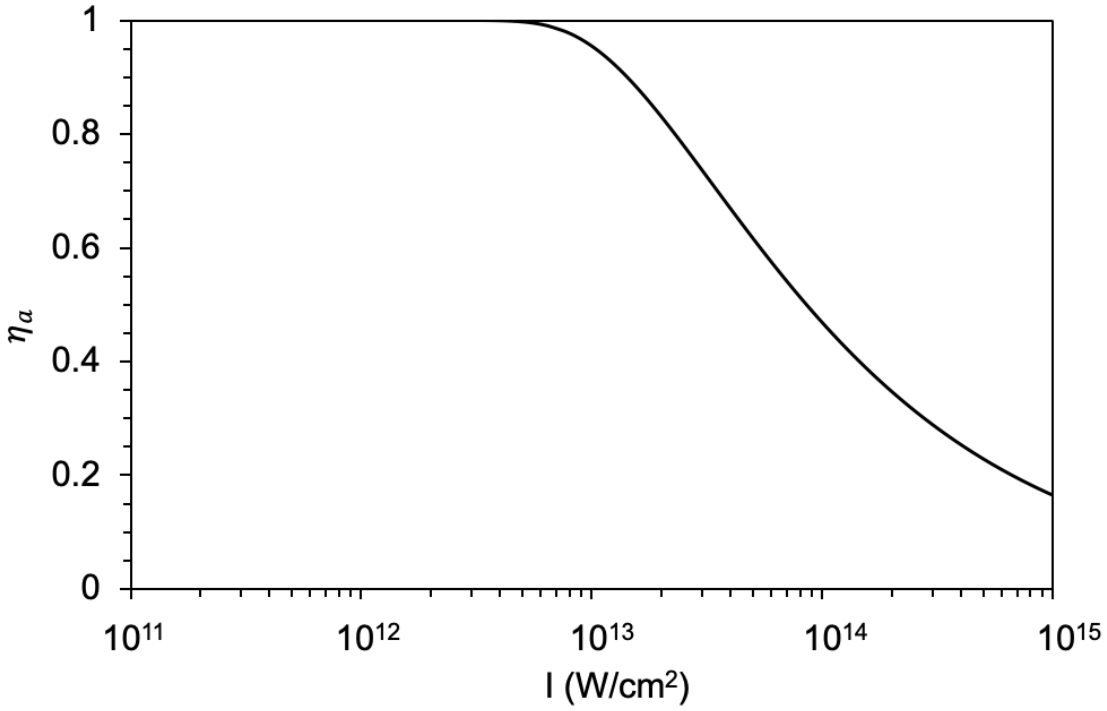

Fig. 2.5 Laser intensity dependence of absorptivity

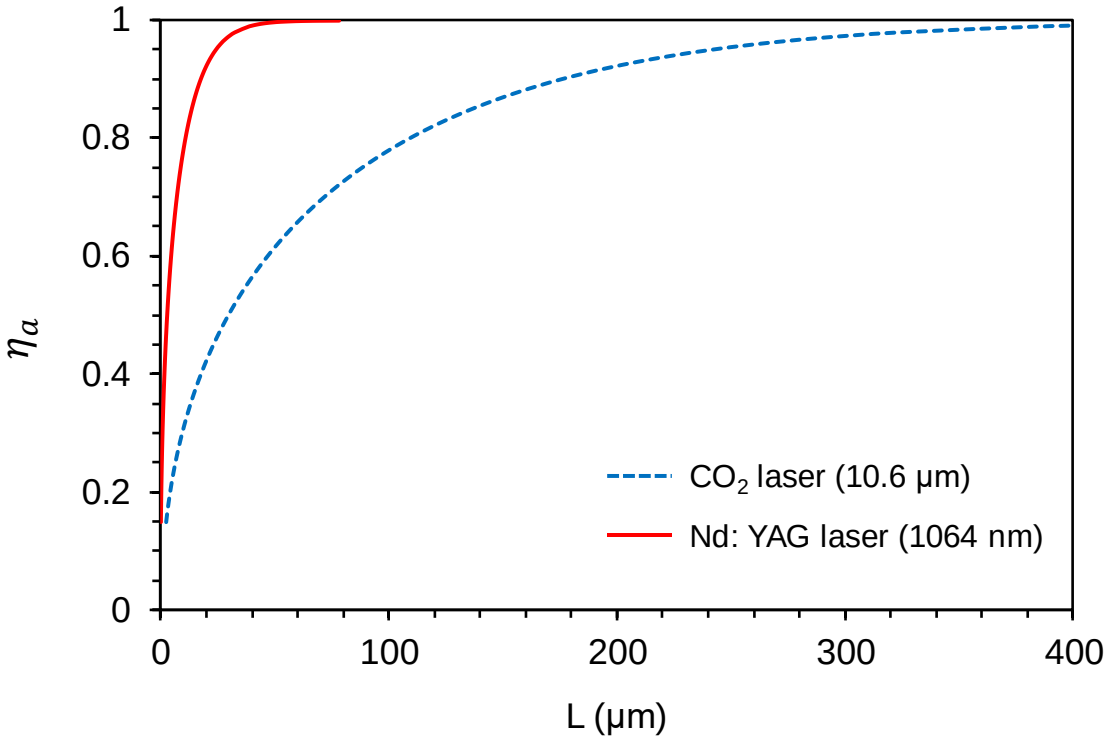

Fig. 2.6 Scale length of electron density dependence of absorptivity of CO_2 laser and Nd: YAG laser

References

[1] K. Tomita, doctoral dissertation, Kyushu University (2013).

[2] D. H. Froula, S. H. Glenzer, N. C. Luhman Jr. and J. Sheffield, Plasma scattering of electromagnetic radiation, Academic press, New York, (2011).

[3] M. Sneep and W. Ubachs, J. Quant. Spectrosc. Radiat. Transfer, 92, 293 (2005).

[4] J. A. Sutton and J. F. Driscoll, Optics Letters Vol. 29, Issue 22, pp. 2620-2622 (2004).

[5] A. F. H. van Gessel, E. A. D. Carbone, P. J. Bruggeman and J. J. A. M. van der Mullen, Plasma Sources Sci. Technol. 21, 015003 (2012).

[6] A. Scheeline and M. J. Zoellner, Appl. Spectrosc. 38, 245 (1984).

[7] D.E. Evans and J. Katzenstein, Rep. Prog. Phys. 32, 207 (1969).

[8] E. E. Salpeter, Phys. Rev., 120, 5 (1960).

[9] K Muraoka, K Uchino and M D Bowden, Plasma Phys. Control. Fusion, 40, 1221 (1998).

[10] 山中千代衛: レーザー工学, コロナ社, Chapter 4 (1981).

[11] T. Yamanaka, the Japan Society of Plasma Science and Nuclear Fusion Research, 69, 6, 2.7 (1993).

[12] A. Sunahara, J. Plasma Fusion Res, 89, 6, 416-422 (2013)

[13] K. Nishihara, A. Sunahara, A. Sasaki, M. Nunami, H. Tanuma, S. Fujioka, Y. Shimada, K. Fujima, H. Furukawa, T. Kato, F. Koike, R. More, M. Murakami, T. Nishikawa, V. Zhakhovski, K. Gamata, A. Tanaka, H. Ueda, H. Nishimura, Y. Izawa, N. Miyanaga and K. Mima, Phys. Plasmas, 15, 056708, (2008).

[14] H. J. Kunze, Plasma Diagnostics, ed. W. L. Holtgreven, Chapter 9, North- Holland publishing company, Amsterdam, (1968).

[15] Z. Xiong, E. Robers, V. Sarron, J. M. Pouvesle and M. J. Kushner, J. Paal. Phys. D: Appl. Phys., vol. 45, p. 275201, (2012).

Chapter 3

Ion feature measurement of EUV light source plasmas

3.1 Introduction

This chapter describes the diagnostic of the laser-produced Sn plasmas for EUV light source produced by Sn droplet targets and a CO_2 laser. A CO_2 drive laser and a Sn droplet target are used as an efficient EUV light source.[1][2] Improvement of the EUV output power is an important issue, as mentioned in chapter 1. As regards practical application, the primary challenge involves the improvement of the conversion efficiency (CE) of EUV light sources with respect to CO_2 lasers, which are used as driving lasers to produce plasmas.[3][4] A double-pulse irradiation scheme is proposed, where a pre-pulse laser expands a small tin droplet, and the CO_2 laser irradiates when it reaches a size of approximately 300 μm in diameter,[5] and a CE of approximately 4% was confirmed using this approach.[6] Consequently, controlling and understanding of Sn plasma behavior are essential, because EUV emission strongly depends on the ionic charge of the Sn plasma.[7][8] In addition, the opacity parameter is not negligible when the plasma density becomes very high.[9][10] Researchers have predicted that the optimum values of the electron density (n_e), electron temperature (T_e), and the average ionic charge (Z) should lie in the ranges of 10^{24}-10^{25} m^{-3}, 30-50 eV, and 10-13,

respectively, to realize high-power EUV light sources with excellent CEs.[11] However, direct measurements of these parameters of laser-produced EUV light source plasmas, whose CE is sufficiently high for practical use, have never been performed. Thus far, we have developed a collective laser Thomson scattering (LTS) system to realize simultaneous measurements of the n_e, T_e, and Z of EUV light source plasmas.

3.2 Development of an ion feature measurement system

In order to diagnose the light source plasmas with a very small size and short lifetime, the diagnostic system with sufficient time and spatial resolutions are indispensable. Specifically, a temporal resolution of about 10 ns and a spatial resolution of 100 μm or below are required. Regarding temporal resolution, the shorter one of probing laser pulse width and the gate width of the detector becomes the time resolution of the diagnostic system.We used an intensified charge-coupled device (ICCD) camera for the detector and the temporal resolution was 5 ns which was the gate width of the ICCD camera. As for spatial resolution, it depends on a spot size of the probing laser for LTS measurements. Decreasing the size of the laser spot improves the spatial resolution, but the possibility of heating the electrons in the plasma increases. The probing laser spot size was determined to be 50 μm.

From the viewpoints of wavelength dispersion and stray light rejection, measurement of electron feature is easier than ion feature. The intensity of the scattered light per unit wavelength of the electron feature is not high and it was difficult to measure in a high electron density situation, because background light was easily overwhelm the electron

feature. Therefore, the ion features of Thomson scattering were detected to measure the n_e, T_e, and Z.

3.2.1 Ion feature spectrum

As shown in 2.2.2, the spectrum and intensity of Thomson scattering have different properties in the case of $\alpha << 1$ and the case of $\alpha > 1$. In a case of the EUV light source plasmas, α is larger than one and the spectral shapes of ion features and electron features reflect the collective behavior of ions and electrons. Ion feature spectrum is scattered light from electrons following ions movement, therefore, it has information of electrons (n_e and T_e) and ions (T_i and Z). The shape of the ion-feature spectrum reflects the ion-acoustic-wave frequency ω_{ac} which can be written as:

$$\omega_{ac} = k\sqrt{\left[\frac{a^2}{1+a^2}\right]\left[\frac{(Z\kappa T_e + 3\kappa T_i)}{m_i}\right]} \tag{3.2}$$

Where κ is the Boltzmann constant, m_i is the ion mass, and T_i is the ion temperature. The spectrum also exhibits two peaks with a dip between them. The width between the two peaks $2\Delta\lambda_{peak}$ is related to the probing laser wavelength λ_0, the speed of light c, and ω_{ac}, and $\Delta\lambda_{peak}$ is expressed as:

$$\Delta\lambda_{peak} = \frac{\lambda_0^2}{2\pi c}\omega_{ac} \tag{3.3}$$

By determining $\Delta\lambda_{peak}$ and the spectral shape, which is characterized by ion-acoustic wave damping, we obtain ZT_e, and T_i. In addition, because the intensity of the scattered light is strongly related to n_e (while weakly depending on T_i and T_e), it is possible to determine n_e by performing the absolute calibration of signal intensity. In this chapter, we assume $T_e = T_i$, and we subsequently determine T_e and Z

3.2.2 Selection of scattering angle and probing laser

The backscattered light of the ion features were measured in this study for the following reasons. The peak width of the ion feature depends on the scattering angle θ_s as shown in Eg. 3.3. Figure 3.1 shows the ion feature spectra of collective Thomson scattering, and the parameter conditions are $n_e = 10^{24}$ m^{-3}, $T_e = 30$ eV, $Z = 10$, θ_s are 45, 90 and 135 degrees. In a view of wavelength decomposition, it is advantageous that the scattering angle is large, as shown in Fig. 3.1. Increasing the scattering angle widens the peak width of the ion feature.

In the experiment of this chapter, Gigaphoton, which is a company developing EUV light source, generated the plasmas. The scattering angle was set to 105 and 120 degrees in the section 3.3 and section 3.4 respectively, due to the relationship of Gigaphoton's plasma production equipment. In the chapter 4, ion feature and electron feature were detected, and the scattering angle was set to 135 degrees for ion feature measurement.

In this study, the second harmonic of the Nd:YAG laser (wavelength $\lambda_0 = 532$ nm) having the following characteristics was used as the probing laser for LTS measurement. First, because the wavelength is in the visible range, it is easy to handle, various kinds of optical components are inexpensive and easy to obtain. Second, high reliability, high

output power, and short pulse width can be easily obtained by the Nd:YAG laser. However, since the required wavelength resolution for spectrometer (20 pm) is comparable to the spectral width of the common YAG laser itself (it is about 25 pm at λ = 532 nm), it is necessary to narrow the wavelength spread by an injection seeder. Third, the energy of the photon is 2.34 eV, which is relatively small in the visible range, and the influence of plasma disturbance by probing laser is also small.

For the above reasons, the second harmonic of the Nd:YAG laser is suitable for measurement of EUV light source plasmas.

3.2.3 Development of a spectrometer

As shown in the Fig. 3.1, since the peak width of the ion feature is below 200 pm, high wavelength resolution is required for the spectrometer. In addition, the spectrum appears near the wavelength of the probing laser and the probing laser reflected by the target surface reaches the detector as stray light. It is necessary to remove only stray light in a very narrow wavelength range. In other words, the wavelength resolution of about 20 pm and the ability to sufficiently remove stray light in a very narrow range, less than ±25 pm, are required. We achieved the required performance by developing an original spectrometer, which improved conventional triple grating spectrometer which gives deep (~ 10^{-6}) notch characteristics for rejecting stray light.[12][13]

Figure 3.2 shows the our original spectrometer mainly consisted of six achromatic lenses (L1–L6, f = 486 mm, effective diameter: 60 mm), five diffraction gratings (G1–G5, 2400 grooves/mm plane holographic reflection gratings with high modulation, effective area: 66 mm height × 75 mm width), an entrance slit (S1, width: 20 μm), an

intermediate slit (S2, width: 20μm), and a thin tungsten wire (diameter: 100μm) to block the stray light, which is referred to as a laser-wavelength stop in this study. An ICCD camera (quantum efficiency: 48% at 532 nm) was used as a detector. The time resolution was determined by the gate width of the ICCD camera and it was set to be 5ns. The basic configuration of the spectrometer is the same as that used in previous studies.[14][15][16]

The part from the entrance slit (S1) to the intermediate slit (S2) plays a role of removing the strong stray light in near measurement laser wavelength. S2 can also remove stray light diffusely reflected on the diffraction grating surface of the spectrometer. The signal after passing through S2 is spectrally separated by final grating (G5) and detected by the ICCD camera. In brief, the substantial spectrometer is only after S2. The reciprocal linear dispersion of the light spectrally dispersed by the diffraction grating can be written as:

$$\Delta\lambda = \frac{d}{mf} cos\theta \tag{3.1}$$

Where $\Delta\lambda$ is reciprocal linear dispersion, d is lattice constant, m is order of diffraction, f is focal length, θ is angle of diffraction. For instance, when the focal length is 486 mm, the number of inscribed lines is 2400/mm, and the diffraction angle is 56.4 degrees (incident angle is 26.4 degrees), $\Delta\lambda$ at the ICCD camera is obtained as 0.47 nm/mm from Eq. 3.1. Since the signal is dispersed by the two diffraction gratings at the laser-wavelength stop position, the value of $\Delta\lambda$ is 0.18 nm/mm. The cut width of the wavelength by laser-wavelength stop is determined by the product of reciprocal linear dispersion (0.18 nm/mm), and sum of slit width of S1 (20 μm) and width of the wire (100 μm). With

this spectrometer, an instrumental width (spectrum resolution) of 18 pm FWHM and a sufficient stray light rejection (~ 10^{-4}) at ±14 pm from λ_0 were achieved.

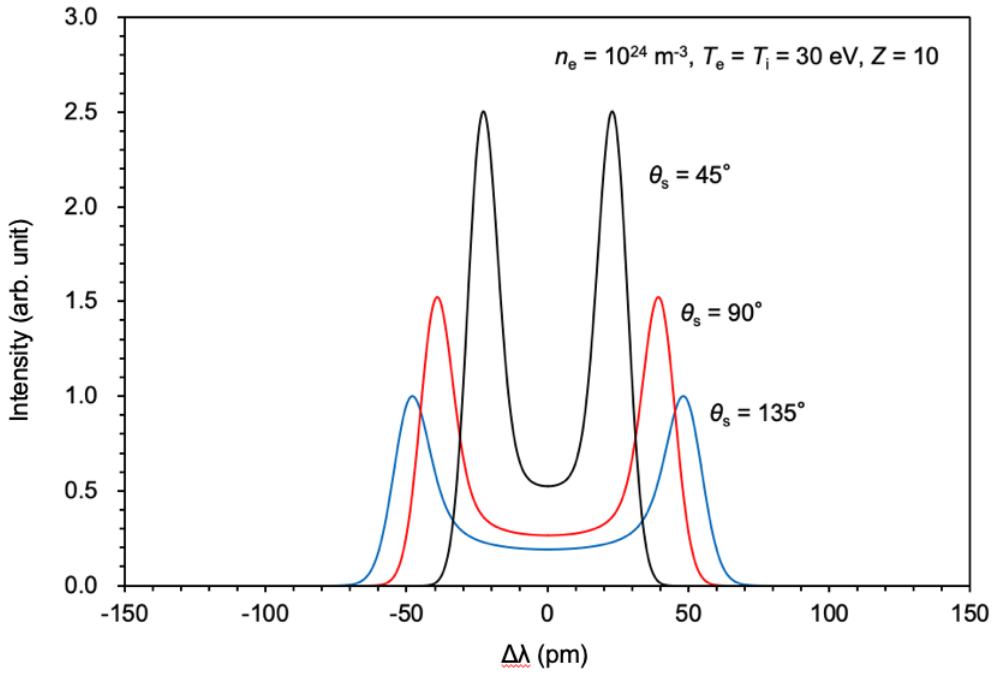

Fig. 3.1 Ion feature spectra at each scattering angle

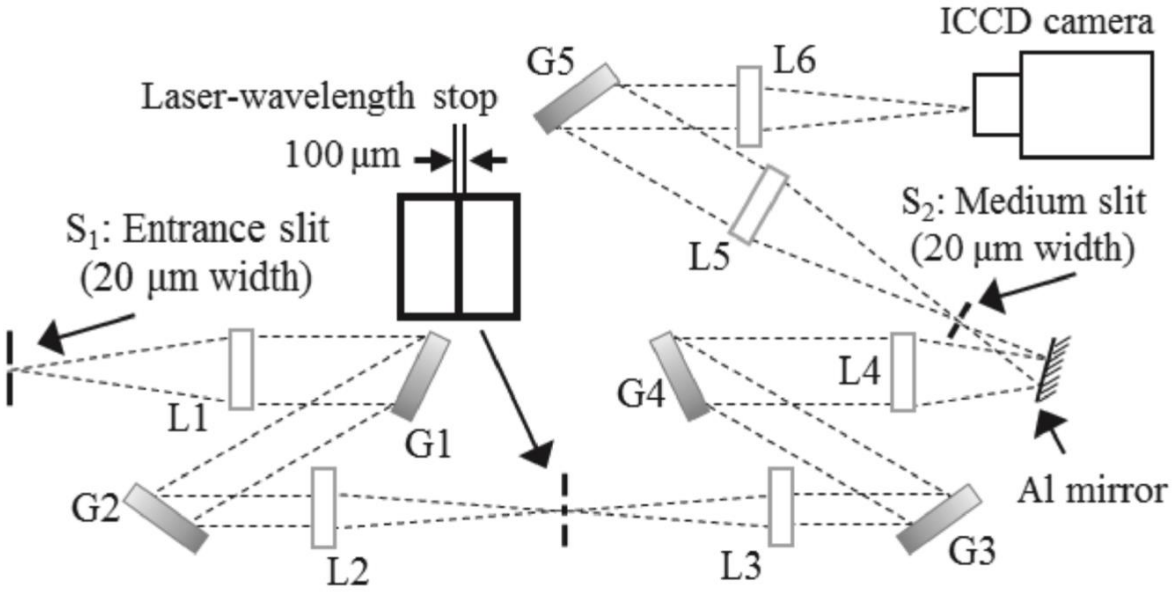

Fig. 3.2 Schematic of a spectrometer having five gratings for detecting ion feature spectra of collective Thomson scattering used in first trial.

3.3 First result of ion feature measurement

3.3.1 Experimental setup

Figure 3.3 shows a schematic diagram of the experimental setup. To generate Sn plasmas, two different lasers were used. One was a fundamental output (wavelength: 1064 nm) from a Nd:YAG laser [pulse width: 10 ns full width at half maximum (FWHM), laser energy: 3 mJ], which was used to crash the Sn droplet target and is referred to as a prepulsed laser in this study. The second laser was a CO_2 laser (pulse width: 15 ns FWHM, laser energy: 100 mJ, wavelength: 10.6 μm), which was used to heat the crashed Sn target and produce the laser- produced Sn plasma. The CO_2 laser is referred to as the main laser. As the probing laser of the laser Thomson scattering (LTS), the second harmonic (wavelength λ_0 = 532 nm) of the Nd:YAG laser (spectral spread <0.1 pm, pulse width: 6 ns FWHM, laser energy: 10 mJ) was used. The Sn droplet of 26 μm diameter was selected as the target material; this target is considered to be a promising candidate for industrial EUV plasmas as a target supplying method with a high repetition rate (>100 kHz).[17] The target was set in a vacuum chamber ($<10^{-4}$ Pa). The prepulsed and main lasers were injected to the Sn target through the same path. The probing laser was injected at 15° with respect to the incident angle of those lasers as shown in Fig. 3.3(b). The typical spot diameters of the prepulsed, main, and probing lasers were 50, 180, and 50 μm FWHM, respectively. The spatial resolution of the LTS measurements was determined by the spot size of the probing laser (50μm). The LTS signals at an angle of 105° with respect to the incident angle of the probing laser were collected and focused on the entrance slit of a handmade spectrometer by lenses. $\boldsymbol{k}_s$ and $\boldsymbol{k}_i$ in Fig. 3.3(b) are the wave vectors of the

scattered light and incident probing laser, respectively. The difference between these wave vectors is defined as $\boldsymbol{k}$. For generating the plasmas, the main laser was injected 6 μs after injecting the prepulsed laser, and the probe laser was injected 15 ns after injecting the main laser. In this study, 0 ns was set as the time when the main laser pulse reached its half-maximum value.

3.3.2 Measurement results

Figures 3.4(a) and (b) show the shadow graphs of the Sn droplet target immediately before injecting the pre-pulsed laser and immediately before injecting the main laser, respectively. Although the initial shape of the Sn target was a sphere of 26 μm diameter, immediately before injecting the main laser, the target expanded and moved.

The Thomson scattering was performed with a single laser shot. Figure 3.5(a) shows the two-dimensional LTS image. Figures 3.5(b)-(d) show the LTS spectra extracted from x = 0.22 (±0.02), 0.34 (±0.02), and 0.52 (±0.02) mm in Fig. 3.5(a), respectively. By using the methods described previously, n_e, T_e (= T_i), and Z were obtained, as shown in Figs. 3.5(b)-(d).[18] Figure 3.6(a) shows the spatial distributions of n_e and T_e, and Fig. 3.6(b) shows the spatial distributions of drift velocity (v_d) and Z. The uncertainties of n_e, T_e, v_d, and Z in Fig. 3.6 were mainly determined by the fitting procedure for the theoretical curves. Figure 3.6(a) also shows the one-dimensional simulation results of n_e and T_e. The LTS results are discussed here. Figure 3.5(a) shows an artificially colored LTS image. In this image, the horizontal axis represents the spatial position (x), and the vertical axis represents the wavelength difference from λ_0 ($\Delta\lambda$). Owing to the laser-wavelength stop, the spectrum near λ_0 ($-14 < \Delta\lambda < 14$ pm) was partially cut. The shift of the entire spectrum

from λ_0 was due to the Doppler shift, which reflects a plasma drift velocity in the direction of $\boldsymbol{k}$.[19] Figure 3.5(a) indicates that the plasma was generated in a range of $0.1 < x < 0.6$ mm. Apparently, this range is larger than that in which the shadow graph of the crashed Sn mist was observed, as shown in Fig. 3.4(b). Moreover, the plasma parameters are clearly different at each position. These facts may reflect the behavior of the Sn plasma, which was heated and expanded by the main laser.

In Figs. 3.5(b)–(d), the typically detected LTS spectra are shown; these spectra are compared with theoretical fitting curves.

3.3.3 Discussions

First, Fig. 3.5(b) shows the spectrum at x = 0.22 mm. This position is the left side of the Sn mist. There is a possibility that the plasma expanded and reached this position. As evidence for this view, the spectrum was Doppler-shifted by -70 pm. This blue shift denotes that the plasma moved in the negative x-direction.

Second, Fig. 3.5(c) shows the spectrum at x = 0.34 mm. At this position, ne reaches the maximum value. Owing to the small Doppler shift and narrow spectral width, the center part of the spectrum was cut, and the depth between the two peaks was not obtained. However, the shape of the spectrum could be fixed. When the spectral width is narrower than this spectrum and spectral peaks are not detected, determining the plasma parameters becomes impossible.

Third, Fig. 3.5(d) shows the spectrum at x = 0.52 mm. This position corresponds to the right side of the crashed Sn mist. The Doppler shift of the LTS spectrum was +40 pm with respect to λ_0. This shift indicates that the plasma moved in the positive x-direction.

As in the case of Fig. 3.5(b), owing to the Doppler shift, the depth between the two peaks of the spectrum was clearly observed, simplifying the fitting procedure.

The LTS system observed the Doppler shift component in the direction of $\boldsymbol{k}$. The v_d values in Fig. 3.6(b) are calculated on the basis of these Doppler shifts. When it is assumed that the plasma expands one-dimensionally along the x-axis, the v_d values become 1.08 times larger than those plotted in Fig. 3.6(b).

In this study, measurements were performed 15 ns after injecting the main laser. Before this time, the intensity of the stray lights markedly increased and easily overwhelmed the LTS signals. Consequently, reliable measurements were difficult. The stray lights might be produced on the surfaces of residual Sn mists, which still remained on the probing laser path. We believe that this problem can be solved by injecting the probing laser on the same path as that of the main laser.

In this study, the lowest T_e was 11 eV. Still, we could analyze the spectrum to obtain T_e. The current data were selected to show the lower detection limit of T_e. For a higher T_e, the analyses become easier because of the broader spectral width.

As part of a future study, reproducing the LTS results by simulation would be useful for optimizing EUV light source plasmas and improving the simulation itself. Here, we performed a one-dimensional radiation hydrodynamic simulation to reproduce the LTS results.[20] The initial ion density (n_i) distribution to the x-axis, which is necessary for the simulation, was estimated from the LTS results. First, the width of the initial plasma was estimated to be 0.1mm FWHM from the shadow graph in Fig. 3.4(b). Next, as per the v_d values shown in Fig. 3.6(b), all the plasmas at $0.1 < x < 0.56$ mm should be condensed within a 0.1 mm width at the initial condition. Under these assumptions, the peak n_i value was estimated to be 3.5×10^{24} m^{-3}. A spatial distribution of n_i to the x-axis

was assumed to have a Gaussian shape. T_e and T_i were assumed to be 0.5 eV. The pulse width of the CO_2 laser was the same as that in the LTS experiment (15 ns FWHM). The input power density was set to 7.8×10^{13} W/m^2 (= 7.8×10^9 W/cm^2), which was three times lower than the experimental condition. When the power density was set to be the same as that in the experiments, simulation results showed a much higher T_e than the LTS results. This discrepancy may have occurred because the simulation was performed using one-dimensional plasma, which is different from the plasma used under real conditions.

The solid lines in Fig. 3.6(a) depict the results of the simulation. As shown in this figure, the simulation shows that T_e lies in the range of 10-15 eV. In addition, even at the peak timing of the CO_2 laser, the maximum T_e is approximately 28 eV, which is lower than that predicted for the optimized EUV light source plasmas (30-50 eV). Next, we changed the initial condition of n_i; although the total number of ions is the same, the FWHM of the ion distribution and the peak n_i were changed to half (0.05 mm FWHM) and double (7.0×10^{24} m^{-3}) the initial values, respectively. As a result, the range of T_e at 15 ns after injecting the CO_2 laser was increased to 15-20 eV, and the maximum T_e at the peak timing of the CO_2 laser was increased to 45 eV. These results indicate that the initial ni condition is important for controlling T_e.

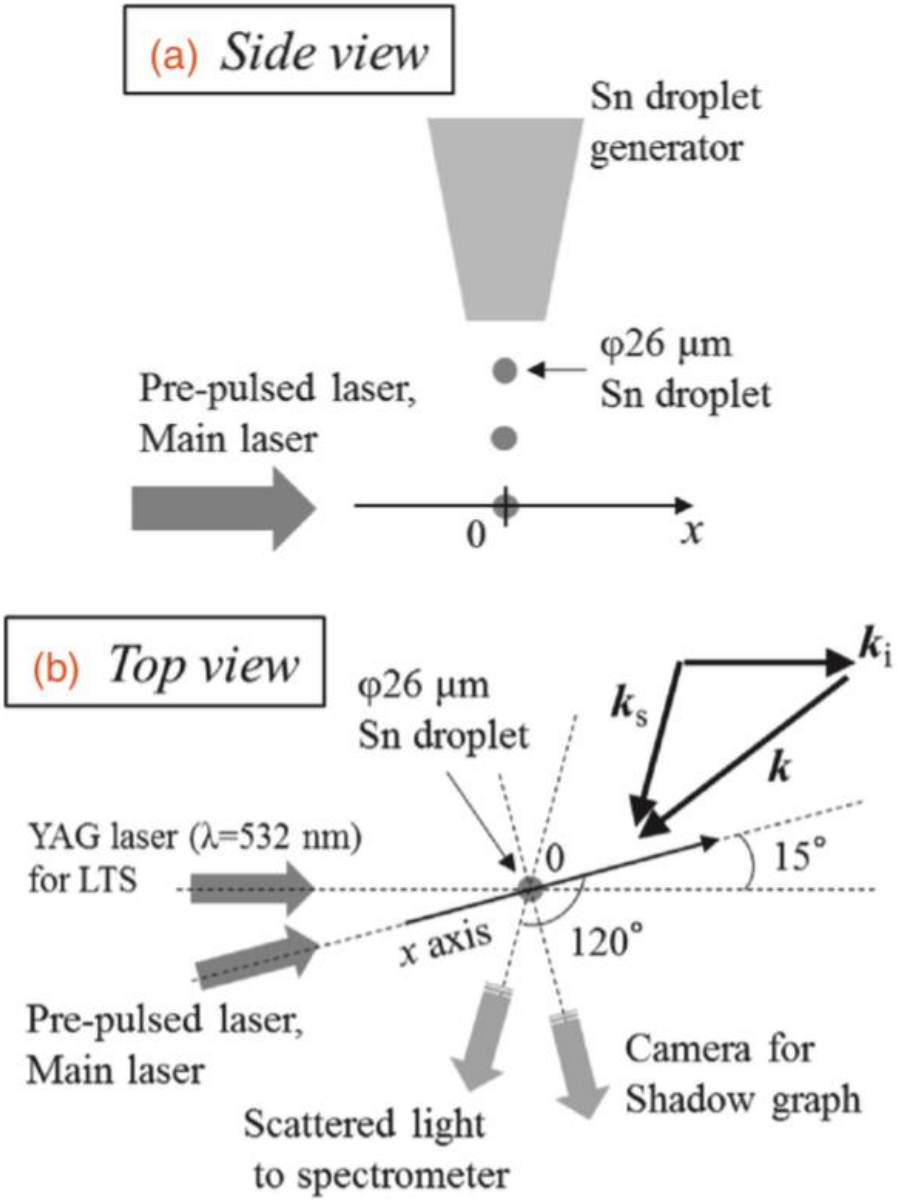

Fig. 3.3 (a) Side and (b) top views of experimental layout.

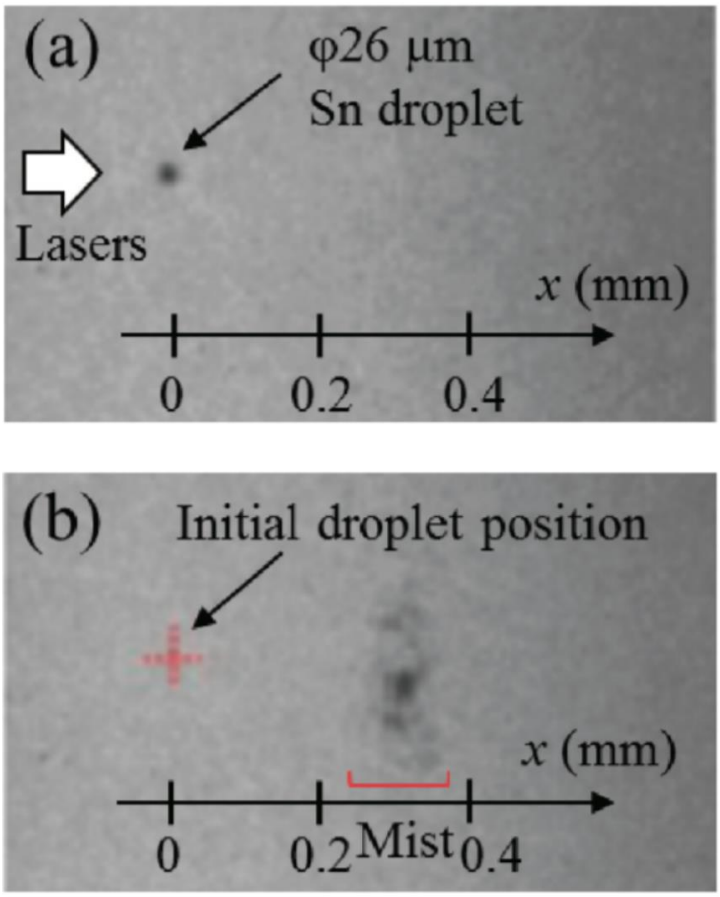

Fig. 3.4 Shadow graph of the Sn droplet target at the times of (a) pre-pulsed laser injection and (b) main laser injection.

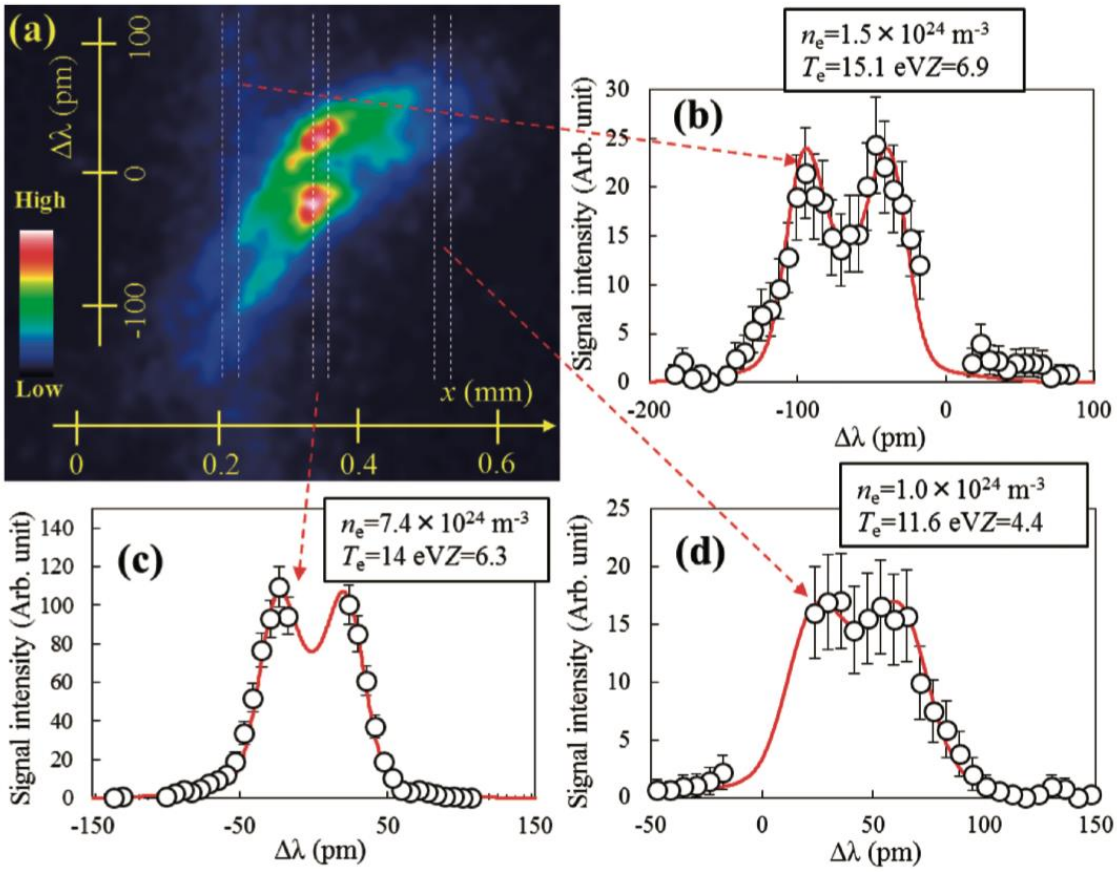

Fig. 3.5(a) Two-dimensional image of ion feature spectrum measured at t = 15 ns. Ion feature spectra at (b) x = 0.22 mm, (c) x = 0.34 mm, and (d) x = 0.52 mm of Fig. 5(a) and their theoretical fitting curves.

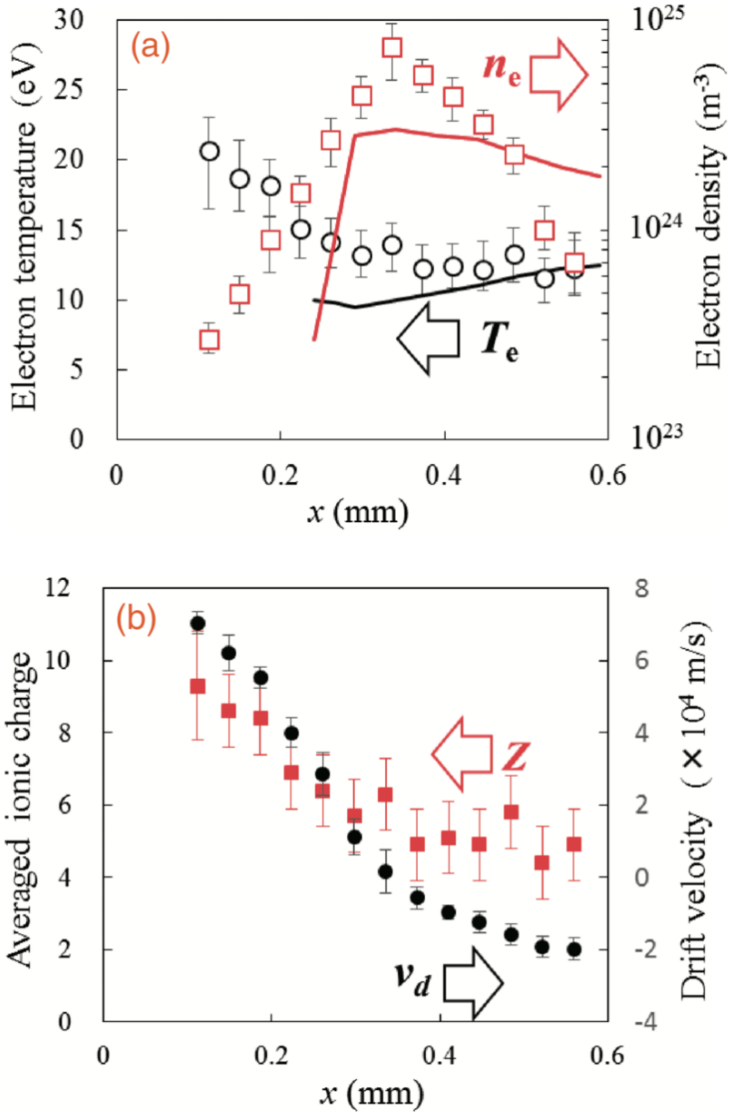

Fig. 3.6 Spatial distribution of (a) n_e and T_e, and (b) v_d and Z obtained from Fig. 3.5(a). The solid lines in (a) show ne and T_e calculated by the one-dimensional radiation hydrodynamic simulation.

3.4 Spatial profiles of the EUV light source plasma parameters

3.4.1 Experimental setup

Figure 3.7(a) schematically shows the experimental setup. A droplet generator supplied the Sn droplet target (diameter: 26 μm) inside a vacuum chamber (<10^{-4} Pa). The pre-pulse and main lasers propagated in the *x* direction and irradiated the droplet. The *x*, *y*, and *z* axes are defined in Fig. 3.7(a), where the droplets fell in the *z* direction. The origin of the coordinate was set to the initial droplet position before the pre-pulse irradiation. The pre-pulse laser was a Nd:YVO_4 laser with a 14 ps pulse width [full width at half maximum (FWHM)], a 2 mJ laser energy at 1064 nm, and a spot diameter of 66 μm ($1/e^2$ intensity) at the droplet position. The diameter of the $1/e^2$ intensity was used for the laser spot size. The main laser was a CO_2 laser with a 15 ns pulse width (FWHM), 100 mJ at 10.6 μm, and a spot diameter of 400 μm. Figure 3.7(b) and (c) show shadowgraphs of the initial tin droplet and that of the expanded tin droplet at 2.0 μs after the pre-pulse irradiation, respectively. Time-integrated, in-band EUV images were observed in the negative *y* axis direction [Fig. 3.7(d)]. The in-band EUV radiation was measured with an EUV energy sensor located at an angle of 150° from the *x* axis [Fig. 3.7(a)]. The probe laser for the CTS was the second harmonic of a Nd:YAG laser with a spectral linewidth below <0.1 pm (FWHM) (pulse width: 6 ns FWHM, 3–10 mJ, wavelength λ_0 = 532 nm, spot diameter of 50 μm in the scattering volume). All three lasers had identical beam paths. The CTS signals were collected by lenses at an angle of 120° from the incident laser direction, focusing on the entrance slit of the spectrometer (20 μm width and 5 mm height) and detected by an intensified charge-coupled device (ICCD) camera (Princeton

Instruments, PI-MAX4, 45% quantum efficiency at λ_0). The spectrometer in this study was similar to that shown in Fig. 3.2. However, to improve the spectral resolution, we used an additional grating in the last section of the spectrometer to increase wavelength dispersion, as shown in Fig. 3.8. With this spectrometer, an instrumental width (spectrum resolution) of 12 pm FWHM and a sufficient stray light rejection ($\sim 10^{-4}$) at ±14 pm from λ_0 were achieved as shown in Fig. 3.9(a)-(c). The x axis dimension of the scattering volume was imaged in the slit height direction. Therefore, one-dimensional, spatially resolved measurements were achieved at the same time.[14, 15] The CTS measurements were repeated over 30 times at identical experimental conditions. The sufficient reproducibility of the spectra was also confirmed. Regarding the plasma heating by the probe laser, the relative temperature increase ($\Delta T_e/T_e$) was discussed in a previous paper[18] based on a model considering the absorption by the inverse bremsstrahlung and of the heat transport to the volume surrounding the laser beam during the laser pulse.[21][22] As a result, ΔTe/Te was estimated to be less than 3% for the cases reported here. The CE for a solid angle of 2π sr was calculated assuming an isotropic distribution of the EUV radiation.

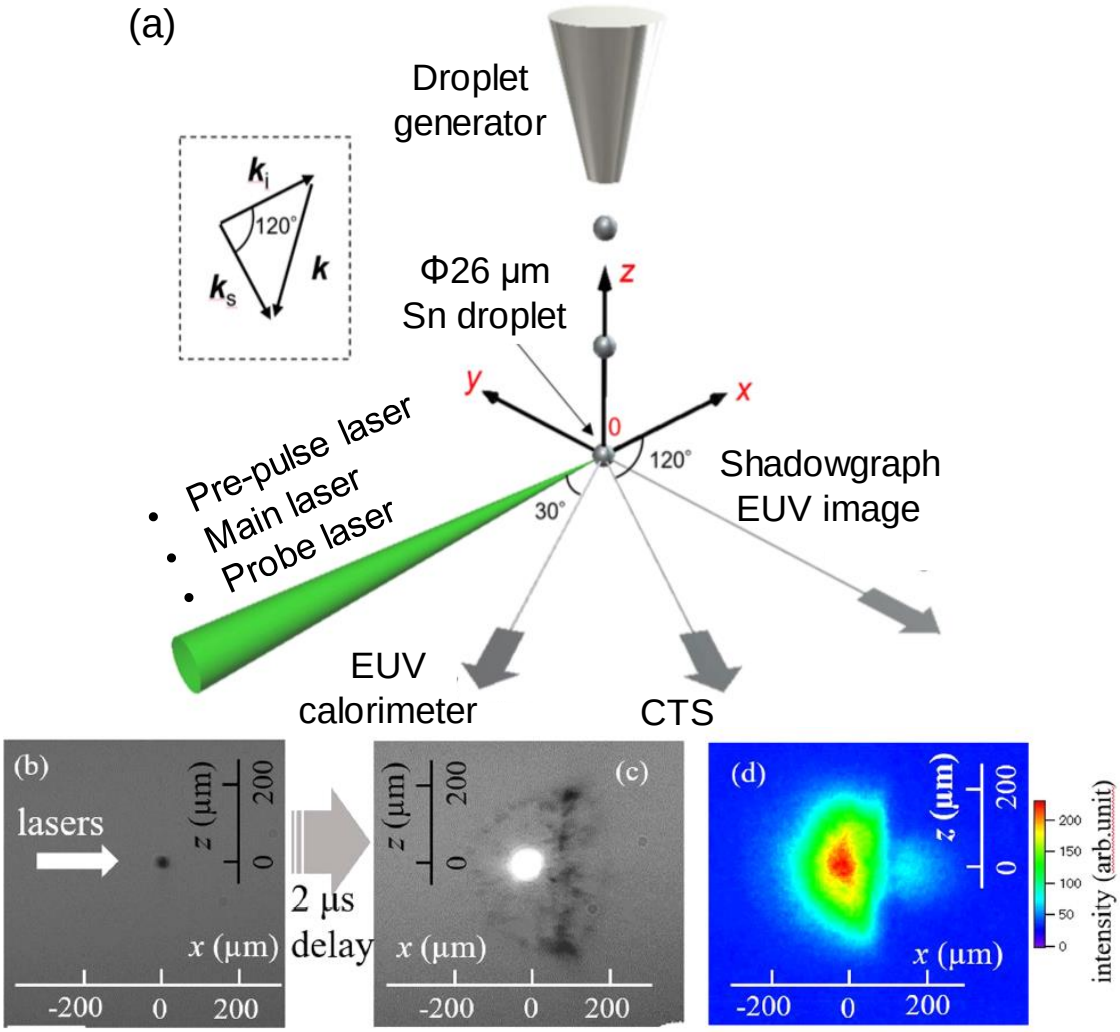

Fig. 3.7 (a) Schematic view of the experimental layout. (b) Shadowgraph of the initial Sn droplet target (φ = 26 μm) and (c) 2 μs after the pre-pulse laser. (d) Image of the EUV emission of the 2.0 μs plasma.

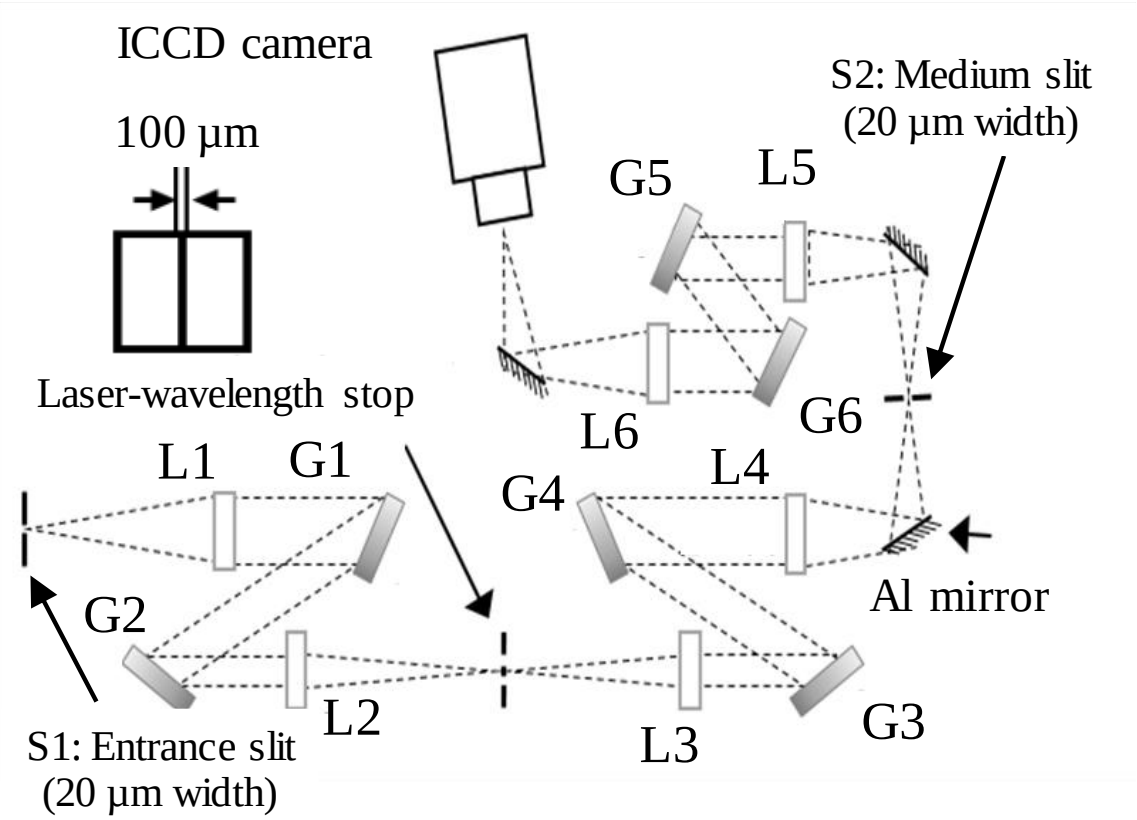

Fig. 3.8 Schematic of a spectrometer having six gratings for detecting ion feature spectra of collective Thomson scattering.

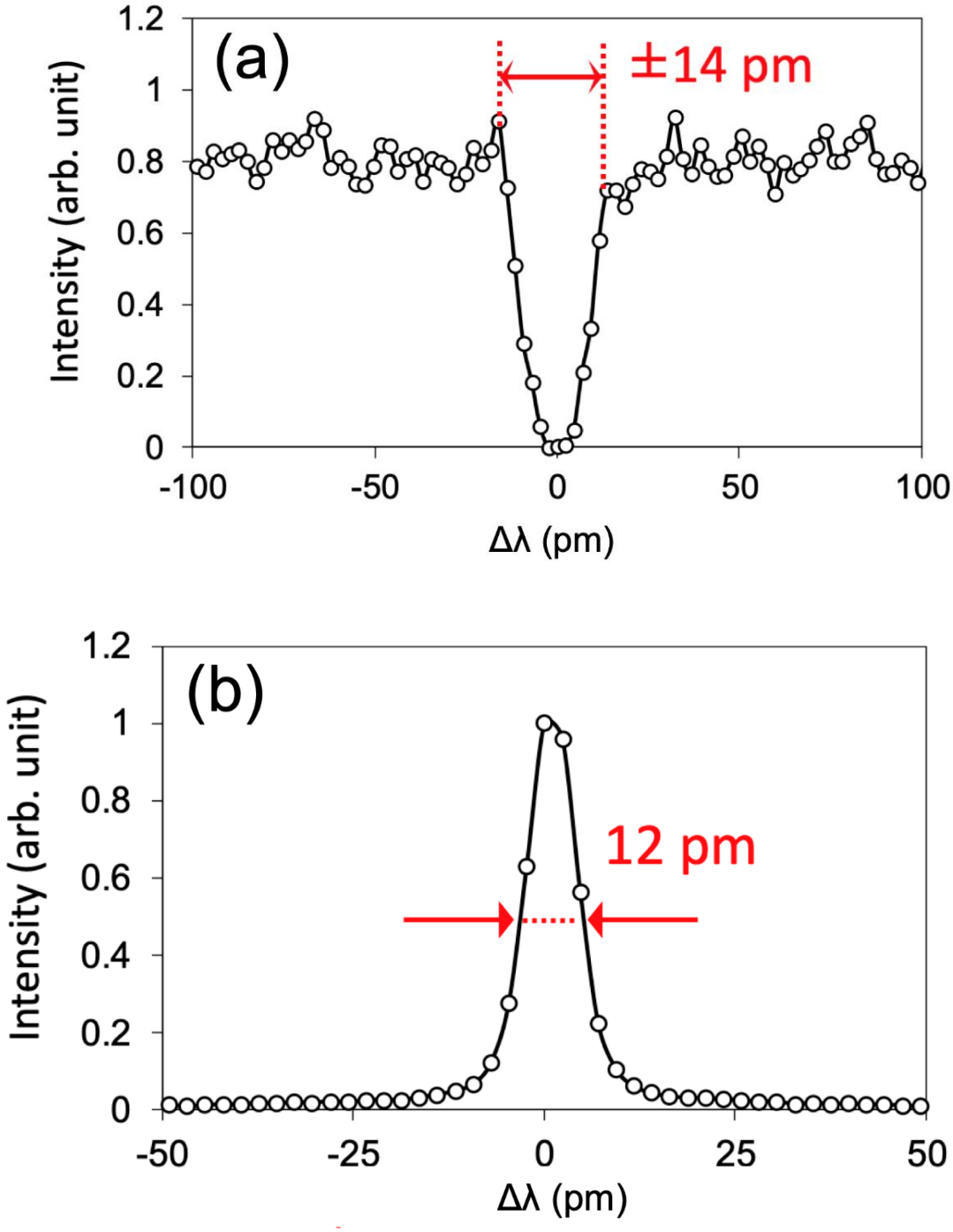

Fig. 3.9 (a) stray light cut width, (b) spectral resolution

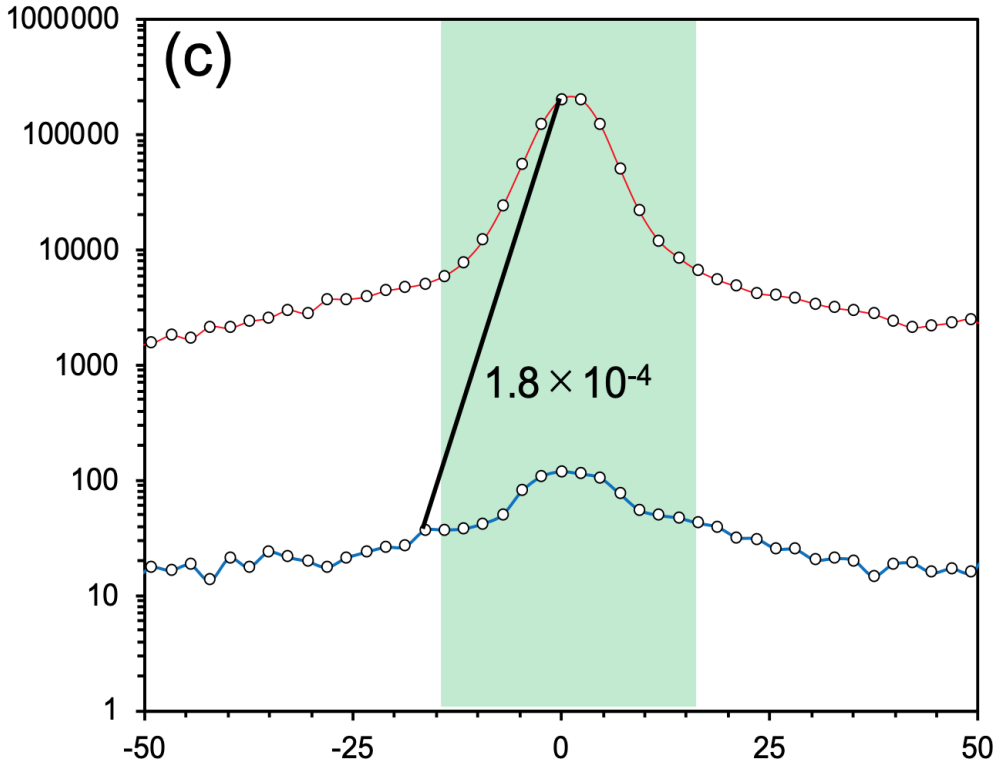

Fig. 3.9 (c) stray light rejection performance of the spectrometer

3.4.2 Two-dimensional plasma parameter profiles

Figure 3.10 shows the typical waveforms of the main and probe lasers. As shown in this figure, the time zero (t = 0 ns) for the CTS measurements was of the first peak of the main laser. The absolute CE measurements showed that the plasma produced at the delay time of t_d = 2.0 μs (hereafter referred to as 2.0 μs plasma) had the maximum CE herein (i.e., 4.0%). The CE values for the 1.3 μs and 2.5 μs plasmas decreased to 3.1% and 2.8%, respectively. These three different plasmas were diagnosed by CTS to investigate the relation between the CE and the plasma parameters. The CTS measurements were performed at 0, 50, 100, 200, and 300 μm in the y axis direction [Fig. 3.8(a)] and at times of t = 5, 10, and 15 ns [Fig. 3.10]. Sufficient symmetry of the plasma along the y-axis was confirmed in the complementary CTS measurements in the negative y-axis (y = −100, −200, and −300 μm) at t = 10 ns. The spatial resolutions of the measurements were 13, 50, and 20 μm for the x, y, and z axis directions, respectively [Fig. 3.8(a)]. These resolutions were determined by the pixel size of the ICCD camera (13 μm), laser spot size (50 μm), and entrance slit width (20 μm). The time resolution was determined by the ICCD camera gate width of 5 ns. Figure 3.11(a) presents a typical, single-probe laser pulse CTS image for the 2.0 μs plasma at t = 10 ns and at y = 0 μm. The horizontal axis in the figure is the x axis (i.e., laser propagation axis), while the vertical axis is the wavelength difference $\Delta\lambda$ from λ_0. The dark area at $\Delta\lambda$ = 0 (within the width of ±14 pm from λ_0) is the discussed wavelength suppression to reduce the stray light.[16] Figure 3.11(b) illustrates the spectrum at 15 < x < 45 μm of Fig. 3.11(a) and its fitting curve. We note that the absolute calibration of the CTS system was performed by Rayleigh scattering measurements from nitrogen gas. The vertical (y-axis) scan of CTS measurements was

performed by moving the focusing position of the probe laser. The absolute calibration of the CTS system was performed at each y position. By using the methods described in the following Method section, n_e, T_e ($=T_i$), and Z were determined as 3.6×10^{24} m^{-3}, 38 eV, and 12, respectively. The shift of the entire spectrum from λ_0 was caused by Doppler shift, which reflected a plasma drift velocity in the k direction of approximately 1.2×10^4 m/s.

Figure 3.12(a) shows the electron density profiles at different y positions from the 2.0 μs plasma at a time of t = 10 ns. Figure 3.12(b)–(d) demonstrate the contour plots of n_e, T_e, and Z in the x–y planes, respectively. Figure 3.12(e) presents the local in-band EUV emissivity ηEUV ($W/m^3/eV/sr$) calculated as a function of x and y from the measured values of n_e, T_e, and Z and the atomic model based on the Hullac code.[8] Intense ηEUV occurred, where a high electron density ($\geq 4 \times 10^{24}$ m^{-3}) and a high temperature (≥25 eV) were simultaneously observed. Note that the plasma cut-off density of the CO_2 laser was 10^{25} m^{-3}. Figure 3.13(a) and (b) show the ηEUV profiles of the 2.0 μs plasma measured at time t = 5 and 15 ns, respectively. By comparing Fig. 3.13(a) and (b) with Fig. 3.12(e), we found that the EUV emission was clearly the strongest at approximately 10 ns. Figure 3.13(c) shows the sum of the ηEUV profiles displayed in Figs 3.12(e) and 3.13(a) and (b). The large emissivity of $\geq 2.5 \times 10^{15}$ $W/m^3/eV/sr$ occurred at approximately y~50–100 μm. The measured EUV image shown in Fig. 3.8(d) has its maximum at y = 0 μm. We calculated the in-band EUV intensity ($W/m^2/eV/sr$) represented in Fig. 3.13(d) from the emissivity profiles [shown in Fig. 3.13(c)] by solving the radiation transport along the line of sight with taking the plasma self-absorption into account under the assumption of the axial symmetry of the plasma profiles. The plasma self-absorption was calculated from in-band opacity represented in Fig. 15(e) of ref. 8. The ray trace method [e.g., ref.

23 and similarly Eq. (8) in ref. 7] was used to calculate the radiation transport. The profiles shown in Fig. 3.8(d) (measured) and Fig. 3.13(d) (calculated using the CTS results) agreed considerably well. For instance, both showed the maximum EUV radiation on the laser axis (y = 0). The calculated EUV image [Fig. 3.13(d)] did not consider the emissivity at times <3 ns. Hence, the EUV image was slightly thinner (narrower) at the laser irradiation side than the measured image in Fig. 3.8(d).

Figure 3.14 represents the shadowgraphs and the spatial profiles of n_e, T_e, and ηEUV of the three plasma conditions (i.e., t_d = 1.3, 2.0, and 2.5 μs) measured at t = 10 ns. Figure 3.14(a)–(c) show the shadowgraphs, while Fig. 3.14(d)–(f) and (g)–(i) demonstrate the ne and T_e profiles, respectively. Figure 3.14(j)–(l) show the η_{EUV} profiles calculated from the corresponding plasma parameters of the three different plasmas. The measured data were interpolated in Fig. 3.1 4(d)–(l). Figure 3.14(e),(h), and (k) use the same data set as in Fig. 3.12(b),(c), and (e), respectively.

Figures 3.15 shows the spatial profiles of drift velocity (v_d) at y = 0 μm. v_d was calculated on the basis of the Doppler shift of the ion feature spectra. In the evaluation of v_d, it was assumed that the plasma expands one-dimensionally along the x-axis.

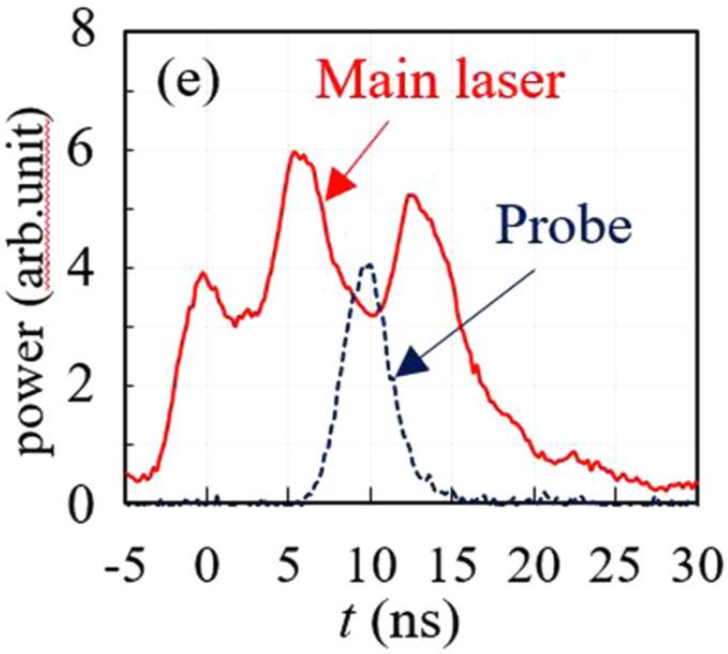

Fig. 3.10 Waveforms of the CO_2 laser and the CTS probe laser.

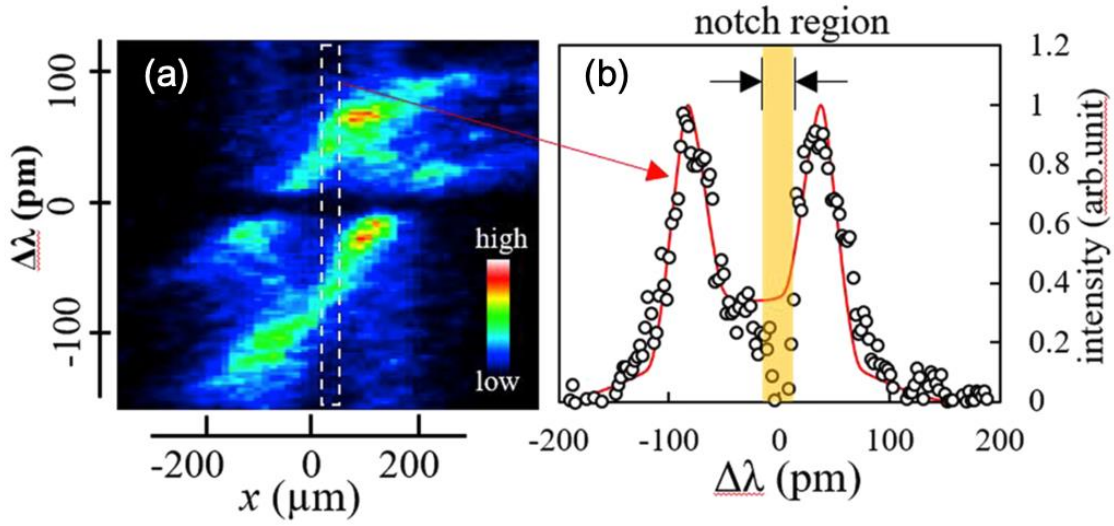

Fig. 3.11 (a) Ion component spectrum measured at time t = 10 ns as a function of x. (b) Ion component spectrum extracted 15 < x < 45 μm of (f) and its theoretical fitting curve.

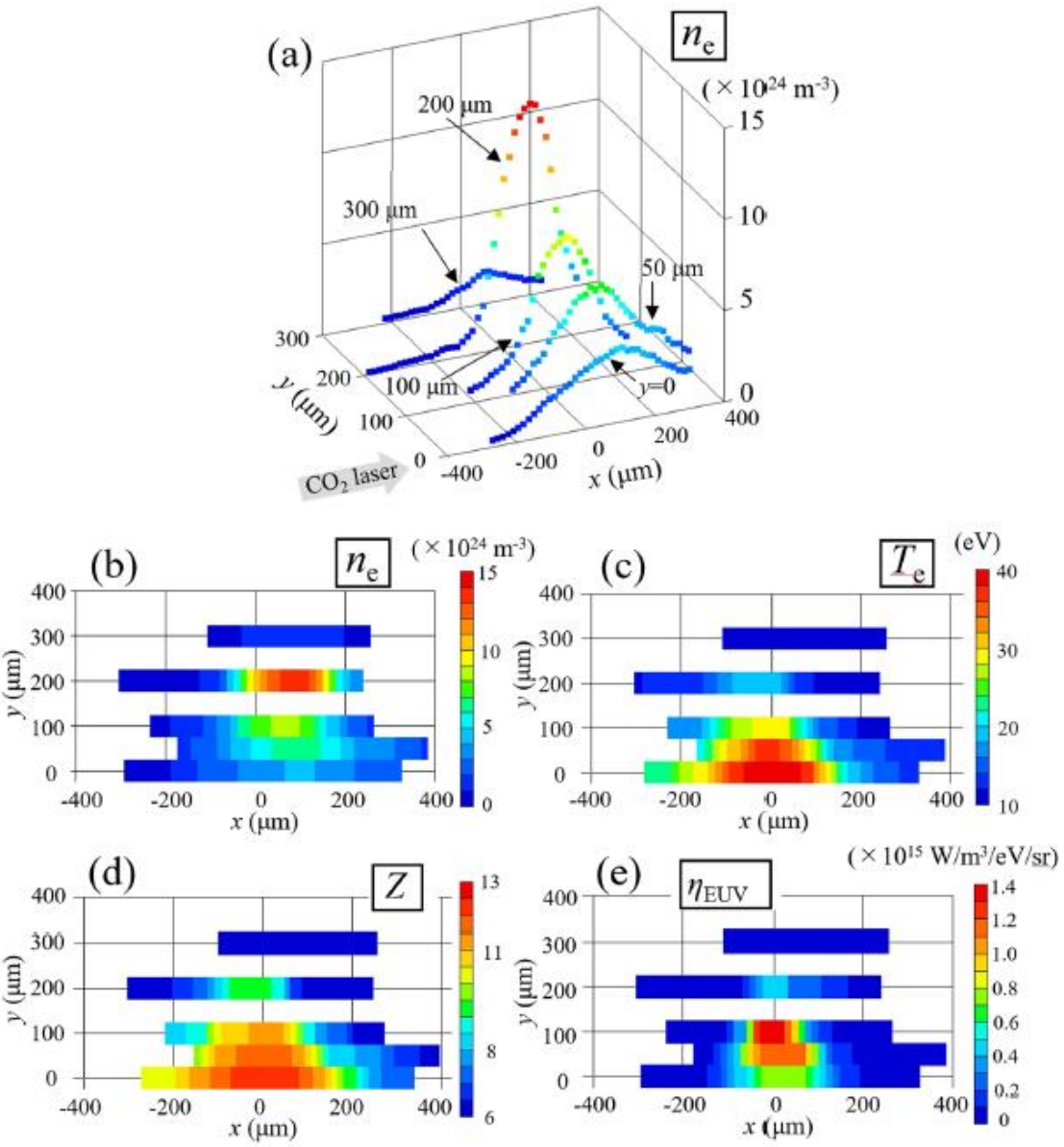

Fig. 3.12 (a) Electron density profiles at y = 0, 50, 100, 200, and 300 μm at time 10 ns. (b,c and d) Contour plots of electron density, electron temperature, and average ionization, respectively. (e) Contour plots of the emissivity obtained from the Hullac code calculation using the CTS data.

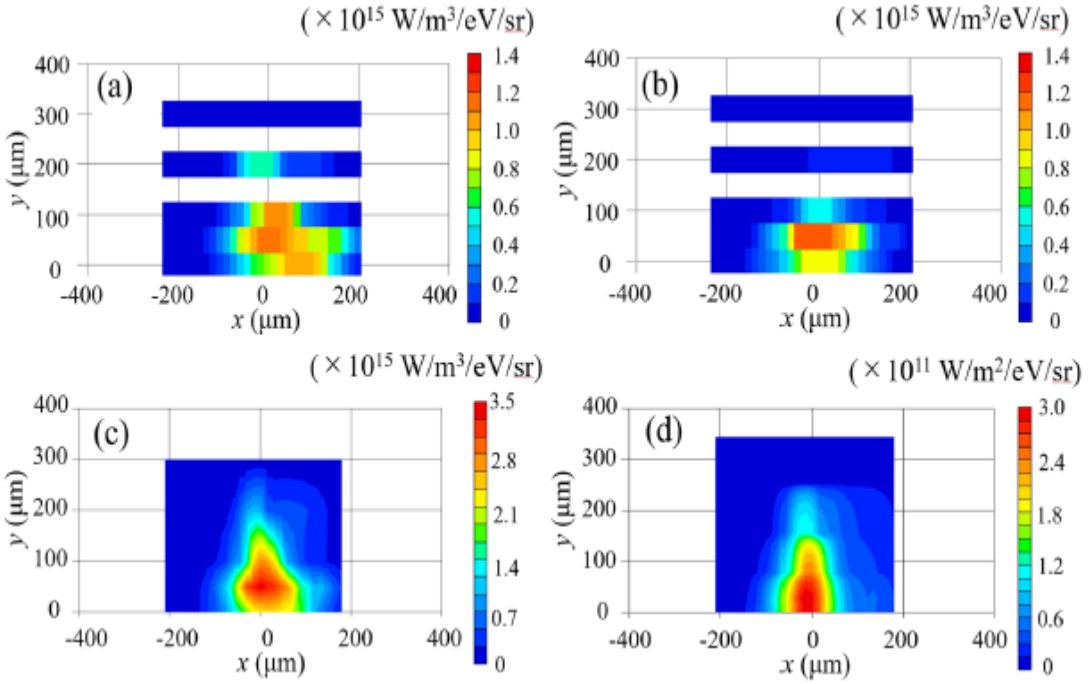

Fig. 3.13(a) Spatial profiles of η_{EUV} at time t = 5 ns and (b) t = 15 ns. (c) Sum of ηEUV obtained from Figs 2(e) and 3(a) and (b). (d) Calculated EUV image obtained by solving the EUV radiation transport with the EUV emissivity shown in Fig. 3(c) with the assumption of the axial symmetry plasma.

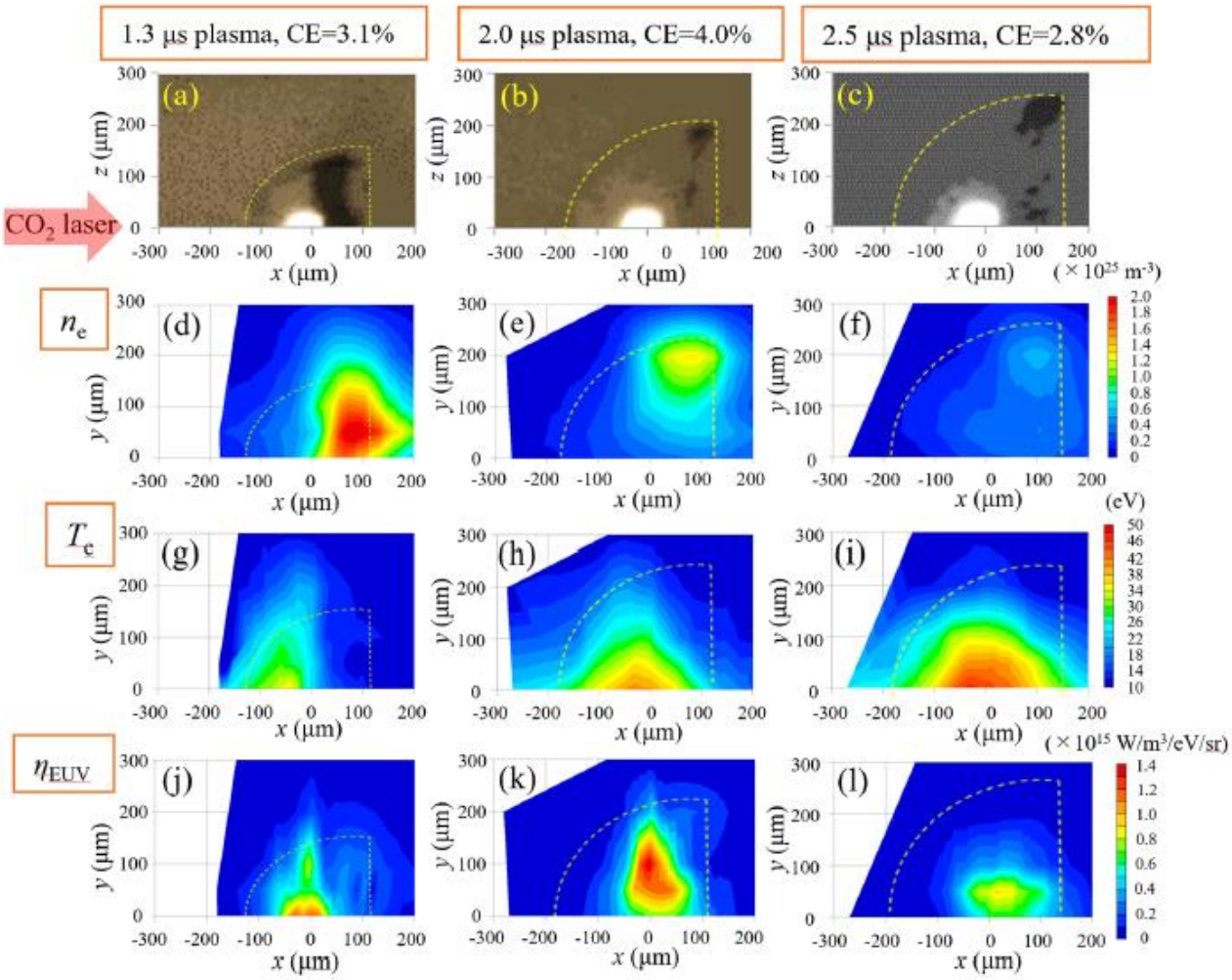

Fig. 3.14(a) Shadowgraph of the 1.3 μs, (b) 2.0 μs, and (c) 2.5 μs plasmas. Similarly, (d)–(f), (g)–(i), and (j)–(l) show the spatial profiles of *n*e, *T*e, and ηEUV of the 1.3 μs, 2.0 μs, and 2.5 μs plasmas at time t = 10 ns, respectively.

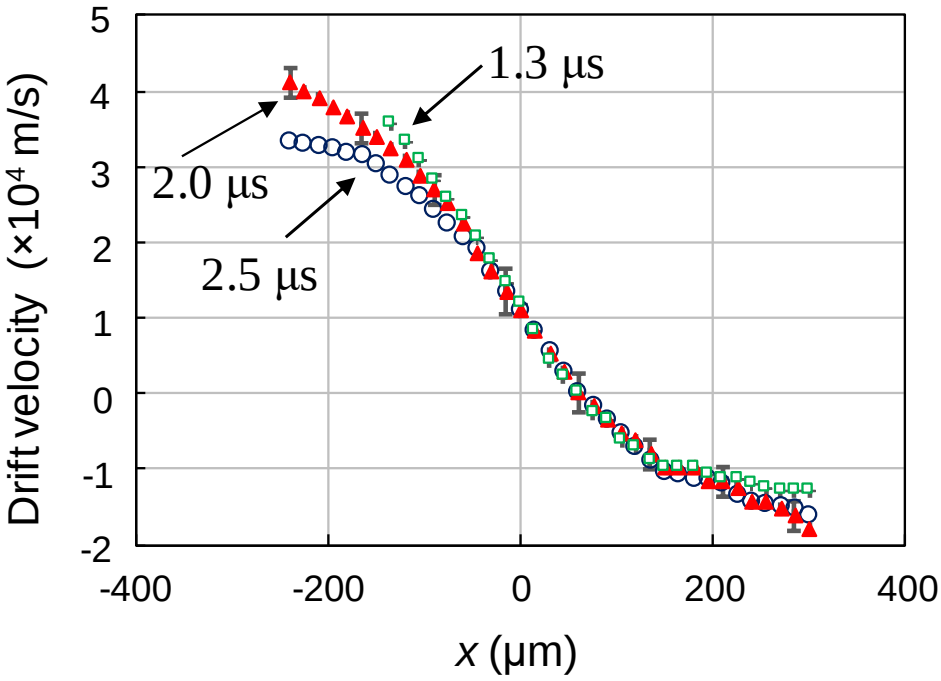

Fig. 3.15 The drift velocity v_d under the three plasma conditions, 1.3, 2.0, and 2.5 μs plasmas

3.4.3 Correlate the parameter profiles and EUV emission

We now discuss the relation between the CE and the spatial profiles of n_e, T_e, and ηEUV for the three plasmas shown in Fig. 3.14(d)–(l). As regards ne, the 1.3 μs plasma exhibited the highest n_e, and the peak n_e reached 2.0×10^{25} m^{-3}, which was larger than the cutoff density of the CO_2 laser (10^{25} m^{-3}). Subsequently, n_e decreased with increasing time delay between the pre-pulsed and main lasers. The observed decrease in n_e can be explained by the decrease in the atomic Sn density of the expanded target.[6] The diameters of the expanded Sn droplet shown in Figs. 3.14(a)-(c) are estimated to be 300, 430, and 530 μm, respectively. Under the assumption of uniform spherical Sn expansion, the average atomic number densities are calculated to be 4.6×10^{25}, 1.6×10^{25} and 8.4×10^{24} m^{-3} for the targets shown in Figs. 3.13(b)-(d), respectively. For the case of the 1.3 μs plasma, the high *T*e (>25 eV) region, in which the tin ion can emit the intense EUV, localized at $x < 0$. In contrast, the high electron density mainly existed at $x > 0$. The high T_e and the high n_e were simultaneously achieved in only the small area at approximately $x = 0$ [Fig. 3.14(d) and (g)]. As is apparent from Fig. 3.14(d) and (e), a large difference in the electron density profile existed between the 1.3 μs and 2.0 μs plasmas. It should be noted that the *y* direction corresponded to the radial one. The plasma also expanded in the radial direction after the pre-pulse laser irradiation. Hence, the Sn density near the *x* axis decreased, and a hollow density profile was formed in the case of the 2.0 μs plasma. We believe that this hollow density profile of the 2.0 μs plasma was a major factor for the high conversion efficiency of 4%. Figure 3.14(j) and (k) show that the maximum EUV emissivity values were almost identical. The maximum values were 1.2 and 1.4×10^{15} $W/m^3/eV/sr$, respectively. However, the high radiation region for the 1.3 μs plasma

existed in only the vicinity of the x axis (i.e., the axis of the laser irradiation), whereas the large emissivity region for the 2.0 μs plasma existed for the radius between 30 μm and 150 μm (i.e., 30 μm $\leq y = r \leq$ 150 μm). The total EUV radiation was given by the volume integration of the emissivity ηEUV. Therefore, the intense emissivity ηEUV at the larger radius mostly contributed to the total EUV radiation. The emitted EUV energy for the 2.0 μs plasma was much larger than that for the 1.3 μs plasma because of the higher emissivity in the region of the larger radius. On the contrary, the region with Te ≥ 25 eV for the 2.5 μs plasma spread in a wide area both in the x and radial directions. However, the maximum emissivity was only 0.9×10^{15} W/m^3/eV/sr. The plasma expanded, and the electron density decreased below 4×10^{24} m^{-3} in the high-temperature region because of the long delay time. We estimated the in-band EUV energies from the emissivity shown in Fig. 3.14(j)–(l) for the three plasma cases under the following assumptions: axial symmetry, isotropic distributions of the EUV radiation, without self-absorption, and an EUV duration of 20 ns. The obtained values were 2.1 mJ, 4.0 mJ, and 1.8 mJ for the 1.3 μs, 2.0 μs, and 2.5 μs plasmas, respectively. Although these values were calculated under the above assumptions, the calculated EUV energies approximately agree with the calorimetric measurements. The details of the difference in the electron density and the temperature between the 1.3 μs and 2.0 μs plasmas can now be compared. A density region higher than the critical density existed for the 1.3 μs plasma at a radius of $r \leq$ 150 μm and an x position of 0 μm $\leq x \leq$ 150 μm. This region has a sharp density gradient near the critical density. As a result, a high-temperature region suitable for the EUV light emission of $T_e \geq$ 25 eV and a high-electron density region (4×10^{24} m$^{-3} \leq n_e \leq 8 \times 10^{24}$ m^{-3}) existed separately. The EUV radiation region was indeed small not only in the radial direction but also in the x direction. On the contrary, both a wide region of high electron

temperature $T_e \geq 25$ eV and high electron density (4×10^{24} m$^{-3} \leq n_e \leq 8 \times 10^{24}$ m^{-3}) existed for the 2.0 μs plasma not only in the *x*-direction but also in the radial direction. Most importantly, the regions of high electron temperature and high density largely overlapped in both directions. In other words, the large volume of the good parameter range was the reason for the high conversion efficiency. Note that ηEUV has a strong nonlinearity with T_e, as shown in Fig. 15(d) in ref. 8. Next, the spatial profiles of v_d are discussed. As shown in Fig. 3.15, the spatial profiles of v_d are almost the same under all conditions. The direction of plasma expansion changed at x=60-70 μm, which corresponds to the dense Sn atom area, as shown in Figs. 3.14(a)-(c). This bipolar expansion of the plasma is similar to a simulation result.[24] Moreover, the v_d values of (1-4) $\times 10^4$ m/s for the forward direction and approximately 10^4 m/s for the opposite direction are well fitted to the simulation result, as shown in Ref. 24. These findings indicate that the TS result reflects the behavior of the laser-produced plasmas with the Sn droplet target.

3.5 Summary

A new LTS system for laser-produced EUV light sources has been developed. With this system, it became possible to acquire the spatial distributions of n_e, T_e, Z, and v_d, along the probing laser path. Concerning T_e, the lower detection limit of 10 eV has been achieved. by using original spectrometer, which achieved 12 pm spectral resolution and sufficient stray light rejection (~10^{-4}) at ±14 pm from λ_0. The spatial resolutions of the measurements were 13, 50, and 20 μm for the *x*, *y*, and *z* axis directions respectively.

It was performed that direct measurements of the n_e, T_e, and Z of laser-produced Sn plasmas for EUVL, whose CEs are 2.8–4.0%, using the collective TS technique. From the collective TS measurements, it becomes possible to compare the EUV emission profiles with the plasma parameters directly, for the first time.

The detailed measurements of the ion feature spectra resulted in the time-resolved two-dimensional spatial profiles of *n*e, *T*e, and *Z*. The two-dimensional plasma profiles of the electron density and temperature significantly changed with the delay time between the prepulse and main lasers; and an electron density of (4–8) × 10^{24} m^{-3} and an electron temperature of ≥ 25 eV were simultaneously observed for the highest CE in the largest plasma volume (i.e., a good plasma structure was obtained).

References

[1] H. Tanaka, A. Matsumoto, K. Akinaga, A. Takahashia, and T. Okada, Appl. Phys. Lett. **87**, 041503 (2005).

[2] G. O'Sullivan and P. K. Carroll, J. Opt. Soc. Am. 71, 227–30 (1981).

References

[3] H. Tanaka, A. Matsumoto, K. Akinaga, A. Takahashi, and T. Okada, Appl. Phys. Lett. **87**, 041503 (2005).

[4] Y. Ueno, G. Soumagne, A. Sumitani, A. Endo, and T. Higashiguchi, Appl. Phys. Lett. 91, 231501 (2007).

[5] S. Fujioka, M. Shimomura, Y. Shimada, S. Maeda, H. Sakaguchi, Y. Nakai, T. Aota, H. Nishimura, N. Ozaki, A. Sunahara, K. Nishihara, N. Miyanaga, Y. Izawa, and K. Mima, Appl. Phys. Lett. 92 (2008).

[6] H. Matsukuma, A. Sunahara, T. Yanagida, H. Tomuro, K. Kouge, T. Kodama, T. Hosoda, S. Fujioka, and H. Nishimura, Appl. Phys. Lett., **107**, 121103 (2015)

[7] K. Nishihara, A. Sunahara, A. Sasaki, M. Nunami, H. Tanuma, S. Fujioka, Y. Shimada, K. Fujima, H. Furukawa, T. Kato, F. Koike, R. More, M. Murakami, T. Nishikawa, V. Zhakhovskii, K. Gamata, A. Takata, H. Ueda, H. Nishimura, Y. Izawa, N. Miyanaga, and K. Mima, Phys. Plasmas 15, 056708 (2008).

[8] A. Sasaki, A. Sunahara, H. Furukawa, K. Nishihara, S. Fujioka, T. Nishikawa, F. Koike, H. Ohashi, and H. Tanuma, J. Appl. Phys. 107, 113303 (2010).

[9] S. Fujioka, H. Nishimura, K. Nishihara, A. Sasaki, A. Sunahara, T. Okuno, N. Ueda, T. Ando, Y. Tao, Y. Shimada, K. Hashimoto, M. Yamaura, K. Shigemori, M. Nakai, K.

Nagai, T. Norimatsu, T. Nishikawa, N. Miyanaga, Y. Izawa, and K. Mima, Phys. Rev. Lett. 95, 235004 (2005).

[10] Y. Tao, H. Nishimura, S. Fujioka, A. Sunahara, M. Nakai, T. Okuno, N. Ueda, K. Nishihara, N. Miyanaga, and Y. Izawa, Appl. Phys. Lett. 86, 201501 (2005).

[11] A. Sasaki, A. Sunahara, H. Furukawa, K. Nishihara, T. Nishikawa, F. Koike, and H. Tanuma, High Energy Density Phys. 5, 147 (2009).

[12] A. Kono and K. Nakatani, Rev. Sci. Instrum., vol. **71**, no. 7, p. 2716, (2000).

[13] K. Tomita, K. Nakayama, K. Inoue, A. Sunahara, and K. Uchino, Appl. Phys. Express **6**, 076101 (2013).

[14] T. Morita, Y. Sakawa, K. Tomita, T. Ide, Y. Kuramitsu, K. Nishio, K. Nakayama, K. Inoue, T. Moritaka, H. Ide, M. Kuwada, K. Tsubouchi, K. Uchino, and H. Takabe, Phys. Plasmas 20, 092115 (2013).

[15] S. Hassaballa, M. Yakushiji, Y. K. Kim, K. Tomita, K. Uchino, and K. Muraoka, IEEE Trans. Plasma Sci. 32, 127 (2004).

[16] K. Muraoka and A. Kono, J. Phys. D 44, 043001 (2011).

[17] T. Yamazaki, H. Mizoguchi, H. Nakarai, T. Abe, Y. Kawasuji, T. Okamoto, H. Tanaka, Y. Watanabe, T. Hori, T. Kodama, Y. Shiraishi, S. Okazaki, and T. Saitou, Proc. SPIE 9422, 94222P (2015).

[18] D. H. Froula, S. H. Glenzer, N. C. Luhmann, Jr., and J. Sheffield, Plasma Scattering of Electromagnetic Radiation (Academic Press, New York, 2011) 2nd ed., Chap. 5.

[19] B. La Fontaine, H. A. Baldis, D. M. Villeneuve, J. Dunn, G. D. Enright, J. C. Kieffer, H. Pepin, M. D. Rosen, D. L. Matthews, and S. Maxon, Phys. Plasmas 1, 2329 (1994).

[20] A. Sunahara, K. Nishihara, and A. Sasaki, Plasma Fusion Res. 3, 043 (2008).

[21] Kunze, H. J. The laser as a Tool for Plasma Diagnostics, in Plasma Diagnostics, edited by W.L. Holtgreven (Amsterdam The Netherlands: North-Holland Publishing Company, 1968).

[22] Spitzer, L. Jr. Physics of Fully Ionized Gases (New York, United States: Dover Publications Inc., 2006).

[23] Zel'dovich, Y. B. & Raider, Y. P. Physics of Shock Waves and High-Temperature Hydrodynamic Phenomena (Dover Publications, Chap. 2, 2012).

[24] V. Sizyuk, A. Hassanein, and T. Sizyuk, J. Appl. Phys. 100, 103106 (2006)

Chapter 4

Observation of the whole Thomson scattering spectrum of laser-produced plasmas for EUV light source

4.1 Introduction

In the study of EUV light sources, as described in chapter 3, measurements of plasma parameters are very important. In order to measure the parameters, a collective laser Thomson scattering (LTS) system, which is tuned to detect the ion feature spectra, has been developed. This system revealed time-resolved two-dimensional profiles of electron density (n_e), electron temperature (T_e), and average ionic charge (Z) of Sn plasmas. Here, we assumed ion temperature (T_i) is equal to T_e. The ion feature is not enough to fix the four parameters, because the ion feature has only three information, i.e., absolute signal intensity, a width between two peaks and a dip between them. In order to evaluate the four parameters without any assumption, simultaneous detections of the ion feature and the electron feature are required. Therefore, we tried to detect both the ion feature and the electron feature of the Thomson scattering spectrum from the plasma which has the parameters of the EUV light source plasma.

To detect both features, there are two things which should be considered. One is differences in spectral widths of the two features. An estimated spectral width of the ion

feature from the typical EUV light source plasma (n_e, T_e, T_i, and Z are 10^{24} m^{-3}, 30 eV, 30 eV, and 10, respectively) is 200 pm. On the other hand, the width of the electron feature is estimated to be 10 nm. To realize simultaneous measurements, we decided to fabricate two different spectrometers which are suitable for the ion feature and the electron feature. The other problem is a very small intensity of the electron feature compared to the noise level of the bremsstrahlung radiation from the plasma. Because the peak wavelength of the electron feature of collective Thomson scattering gives information about the electron density and the electron temperature, we concentrated to detect the peak wavelength of the electron feature in this study. By optimizing the scattering geometry, we finally succeeded to detect the peak of the electron feature with the signal-to-noise ratio larger than one.

4.2 Development of an electron feature measurement system

4.2.1 Electron feature spectrum

The peak wavelength of electron feature depends on the electron plasma frequency. The electron feature spectrum is characterized by two peaks, and the angular frequency at which the peak appears is expressed as:

$$\Delta\omega = \sqrt{\omega_p^2 + \frac{3\kappa T_e k^2}{m_e}} \tag{4.1}$$

Where, ω_p is electron plasma frequency and written as:

$$\omega_p = \sqrt{\frac{n_e e^2}{m_e \varepsilon_0}} \tag{4.2}$$

Where ε_0 is the dielectric constant of vacuum. Here, letting $\Delta\lambda_{\text{peak}}$ be the wavelength at which the electron feature peak appears, it can be written as follows. (λ_0 is 532 nm)

$$\Delta\lambda_{\text{peak}} = \frac{\lambda_0^2}{2\pi c}\Delta\omega = \sqrt{0.719 n_e + 6.65 T_e sin^2 \frac{\theta}{2}}$$

Where, θ is scattering angle. The spectral shape of electron feature is determined by Γα, as shown in 2.2.2, and α depends on n_e and T_e. Therefore, the n_e and T_e are generally determined from the shape and peak wavelength of electron feature. However, in the case of this study, the n_e, T_i, and ZT_e can be estimated by the ion feature, and the T_e can be determined by the n_e and the peak wavelength of electron feature. This is because the whole shape of the electron feature cannot be detected due to intense radiation from the plasma.[1][2][3] Then, efforts were concentrated to detect the peak wavelength of the electron feature.

4.2.2 Scattering angle and a spectrometer

The ion feature was detected by the measurement system used in chapter 3. The scattering angle of ion feature was set to 135 degrees as described in section 3.2.2. Here, the scattering angle of electron feature is decided.

Figure 4.1 shows electron feature spectra of collective Thomson scattering, and the parameter conditions are $n_e = 10^{24}$ m^{-3}, $T_e = 30$ eV, $Z = 10$, θ_s are 55, 90 and 135 degrees. As shown in the Fig. 4.1, increasing the value of α by decreasing the scattering angle is advantageous for peak detection of electron features. However, if the value of α is too large, the total signal intensity decreases, therefor the value of α must be kept within the range of 2-3. For above reason, the scattering angle was set to 55 degrees in this study.

Figure 4.2 shows a triple-grating spectrometer (TGS) which was used for electron feature measurement.[4][5] The TGS mainly consisted of six achromatic lenses (L1: f = 250 mm, L2-L5: f = 170 mm, L6: f = 220 mm effective diameter: 46 mm), three diffraction gratings (1200 grooves/mm, effective area: 56 mm × 56 mm), an entrance slit (width: 60 μm), an intermediate slit (width: 200 μm), and a thin tungsten wire (diameter: 500 μm) to block the stray light. The ICCD camera (quantum efficiency: 45 % at 532 nm, gate width: 2ns) was used as a detector. Two polarized beam splitters were installed between G3 and the ICCD camera. With the TGS, an instrumental width of 0.37 nm and a sufficient stray-light rejection at ±1.5 nm from λ_0 were achieved.

4.3 Experimental setup

Figure 4.3 shows a schematic diagram of the experimental setup. The x, y, and z axes are defined in Fig. 1. Two different lasers were used to generate plasma. A first laser was a Nd:YAG laser (Continuum Surelite II, pulse width: 10 ns full width at half maximum (FWHM), laser energy: 320 mJ, wavelength: 1064 nm, typical spot diameter: 200 μm) and propagated in the z axis. Sn plasma was produced by the first laser. A second laser

was also a Nd:YAG laser (Continuum Surelite II, pulse width: 10 ns full width at half maximum (FWHM), laser energy: 320 mJ, wavelength: 1064 nm, typical spot diameter: 80 μm), which was used to heat the plasmas. In this paper, we refer to the first and the second lasers as the driving laser and heating laser, respectively. After the Sn plasma was heated by the heating laser, a probing laser was injected into the plasma for LTS measurements. The probing laser was a second-harmonic Nd:YAG laser with injection seeding (Continuum Powerlite 9010 with an injection seeder; spectral spread <0.1 pm, pulse width: 8 ns FWHM, laser energy: 10 mJ, wavelength λ_0 = 532 nm, typical spot diameter: 50 μm). The time zero (t = 0 ns) for the LTS measurements was the peak of the driving laser. The heating and the probing lasers were injected at t = 97 ns and t = 100 ns, respectively. The two lasers were injected co-axially along the x axis and were focused at the same position above the target surface by an achromatic lens with the same focal length (f = 150 mm). A tin plate target was set in the vacuum chamber (<10^{-2} Torr) at z = -150 μm and a thin edge face (thickness 100 μm) was used as the laser-irradiated surface. This thickness was selected so as to reduce the amount of the plasma self-emission.

The ion feature and the electron feature were collected by two different achromatic lenses at angles of 135° and 55° with respect to the incidence angle of the probing laser, respectively, as shown in Fig.1. Then, the LTS signals were focused on the entrance slit of the two spectrometers for the ion feature and the electron feature. The spectrometer for the ion feature was same as that described in Fig. 3.8. The gate width of a detector, which was an ICCD camera (quantum efficiency: 35% at 532 nm), was set to 3 ns.

4.4 Results and discussions

Figure 4.4(a) shows the ion feature image detected by the ICCD camera. Figure 4.4(b) shows the LTS spectrum extracted from the Fig. 4.4(a). The spectrum was successfully fitted by a theoretical curve, as shown in Fig. 4.4(b). From the fitting curve and the absolute calibration, n_e, ZT_e, and T_i were fixed to be 1.0×10^{24} m^{-3}, 271, and 25 eV, respectively.

At the final stage of the spectrometer for the electron feature was divided into 2 optical paths using a polarization beam splitter. Both signal beams were focused on an ICCD camera. The vertically polarized beam contained the plasma self-emission spectrum including the electron feature and its image is shown in Fig. 4.5(a). The horizontally polarized beam contained the plasma self-emission spectrum alone and its image is shown in Fig. 4.5(b). It must be noticed that the transmission efficiency of the spectrometer for the vertically polarized lights are about 2 times larger than that for the horizontally polarized lights. Therefore, the intensity spectrum for Fig. 4.5(b) was corrected by this factor and compared with that for Fig. 4.5(a) in Fig. 4.5(c). From Fig. 4.5(c), it can be seen that the intensity of the spectrum from Fig. 4.5(a) is slightly larger than that from Fig. 4.5(b) at around $\Delta\lambda$ =13 nm. Figure 4.5(d) shows a spectrum obtained by the subtraction of the two spectra. The T_e was decided from the peak wavelength of Fig. 4.5(d) and the n_e estimated by the ion feature as the first step. Since the scattered light intensity of the ion feature weakly depends on T_e, several iterations were required to decide the values of n_e and T_e. Finally, n_e, T_e, T_i, and Z were decided to be 1.3×10^{24} m^{-3}, 33 eV, 25 eV, and 8.2, respectively.

First, it was confirmed whether the electron feature intensity shown in Fig. 4.5(d) is consistent with the intensity of the ion feature. As described before, each intensity is proportional the dynamic form factors, therefore a ratio of the calibrated signal intensity must be equal to the ratio between S_i and S_e. Since the ion feature and the electron feature were detected by different detectors, absolute calibration was performed by Rayleigh scattering. As a result of the comparison, the signal intensity of the electron feature was about half of what was anticipated. We found that this is due to the vignetting reduction in the spectrometer and confirmed that the signal intensity at the $\Delta\lambda$ = 12 nm becomes about half of the signal at the center wavelength. Therefore, we conclude that the observed electron feature is plausible.

Second, the signal-to-noise ratio (SNR) of the electron feature is considered. When the present ICCD camera is used as the detector, a portion of the photons illuminating the photo-cathode is converted to photo-electrons (pe), which are accelerated toward the micro-channel-plate (MCP). These multiplied electrons impinge on a phosphor screen and they emit photons. These multiplied photons are converted to electrons by the charge-coupled-device (CCD). The electronic gain through the MCP is estimated to be as high as 10,000. Finally, a single photo-electron is output as 400 analog-to-digital units (ADU). Here, we calculate the number of photo-electrons detected under the measurements of the electron component of Thomson scattering. As shown in Fig. 4.5, the peak intensity of the electron component observed at around $\Delta\lambda$ = 12 nm was 6000 ADU. This signal intensity is equivalent to 15 pe. The dominant noise, in this case, is the shot noise which is due to the statistical fluctuation of single photo-electrons and is determined by the square root of the pe number. As shown in Fig. 4.5(c), the total signal intensity of the plasma radiation at $\Delta\lambda$ = 12 nm is the order of 30,000 ADU. The shot noise based on both

the Thomson scattering and the plasma radiation is calculated to be 11 pe. Therefore, the SNR is higher than one.

Third, we checked the value of T_e obtained by this experiment. The results show that T_e was 1.3 times higher than T_i. To discuss the validity of the difference, the electron heating by absorbing the probing laser (λ = 532 nm) is estimated. The method to evaluate the increment of T_e has been already discussed in previous papers[6][7][8][9], in which the processes of energy absorption by the inverse-bremsstrahlung and the heat diffusion to the volume surrounding the laser beam. Based on the calculations shown in Ref. 6, 7, it is found that an increase in T_e is at most 0.3 eV, which is less than 1% of the measured T_e. Then, we concluded that the effect of electron heating via the probing laser can be negligible.

Therefore, we finally concluded the signal observed here is really that of electron feature and gives a proper value of T_e to be 33 eV.

4.5 Summary

In this study, the ion feature and the electron feature of the laser-produced Sn plasma having parameters necessary for EUV light sources were detected simultaneously for the first time. The electron feature was observed with a SN ratio more than one, and found to be consistent with the ion feature giving a proper value of T_e.

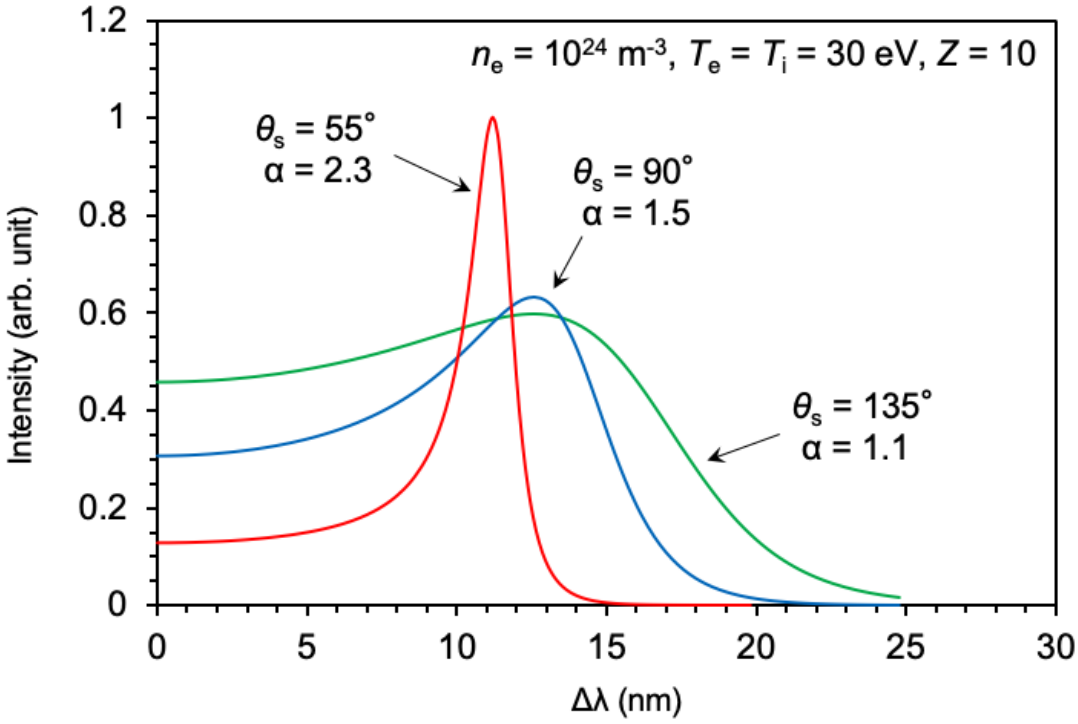

Fig. 4.1 Difference in electron feature spectra due to scattering angle

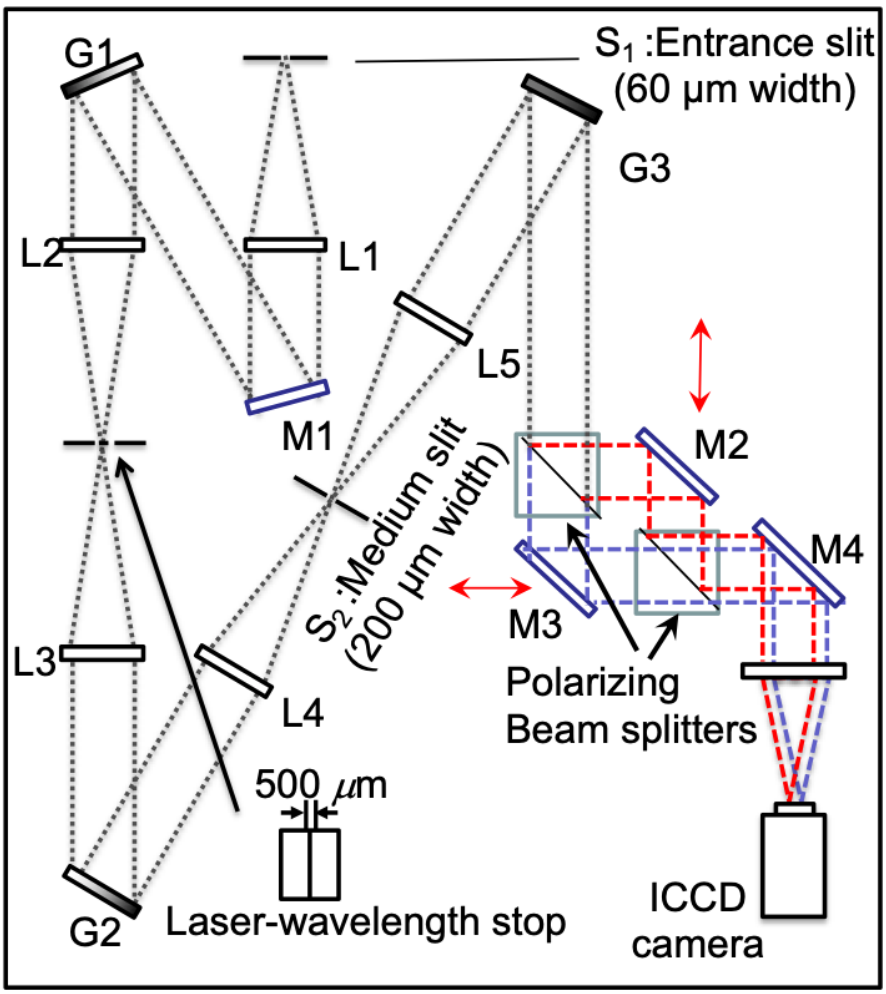

Fig. 4.2 Spectrometer for electron feature measurement

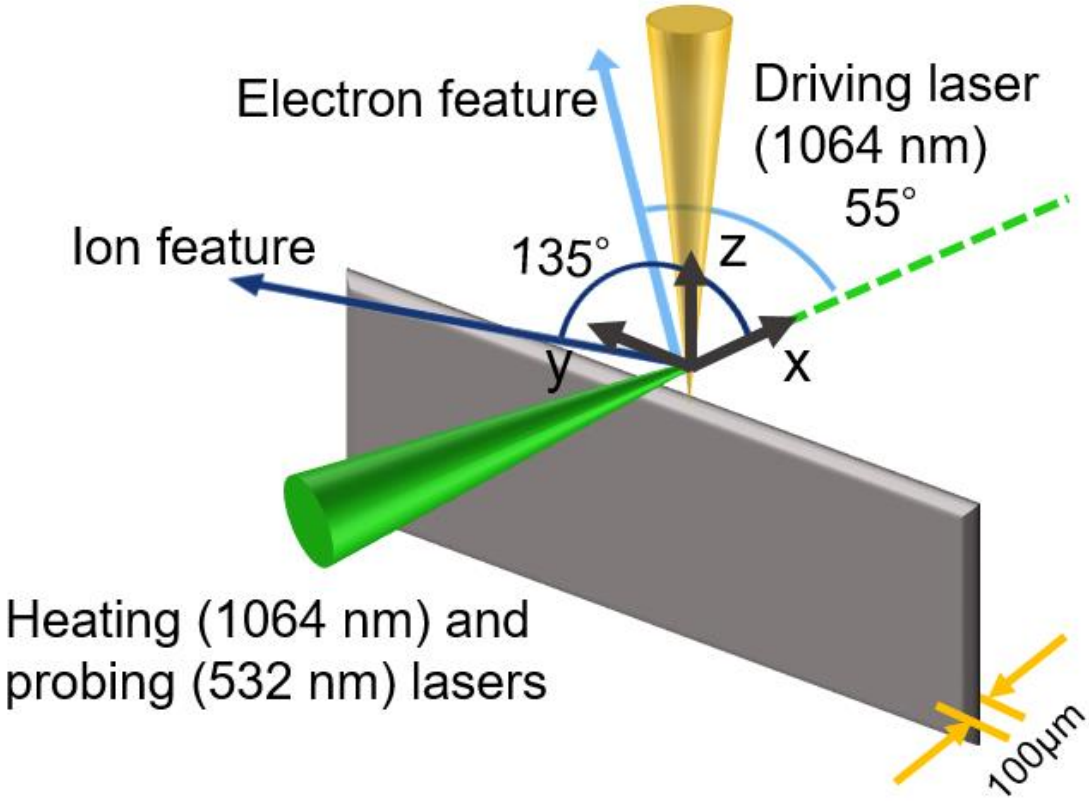

Figure 4.3 Schematic diagram of experimental setup

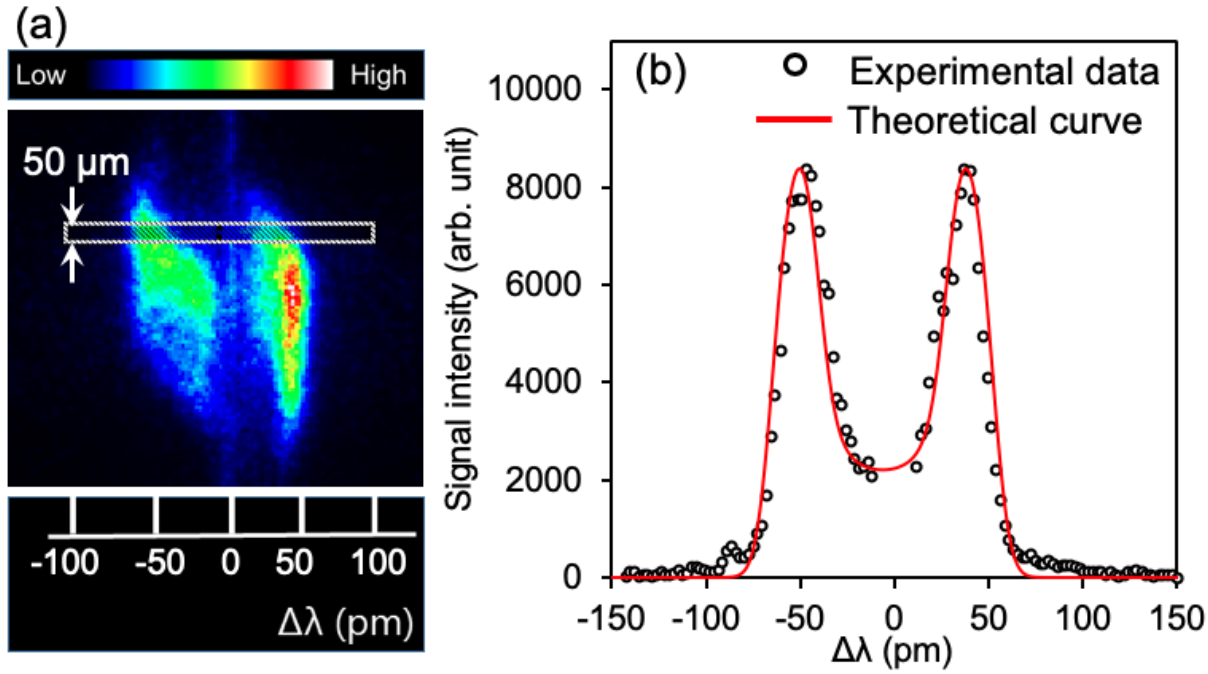

Fig. 4.4 (a) Ion feature image, (b) ion feature spectrum extracted from (a) and the theoretical curve fit

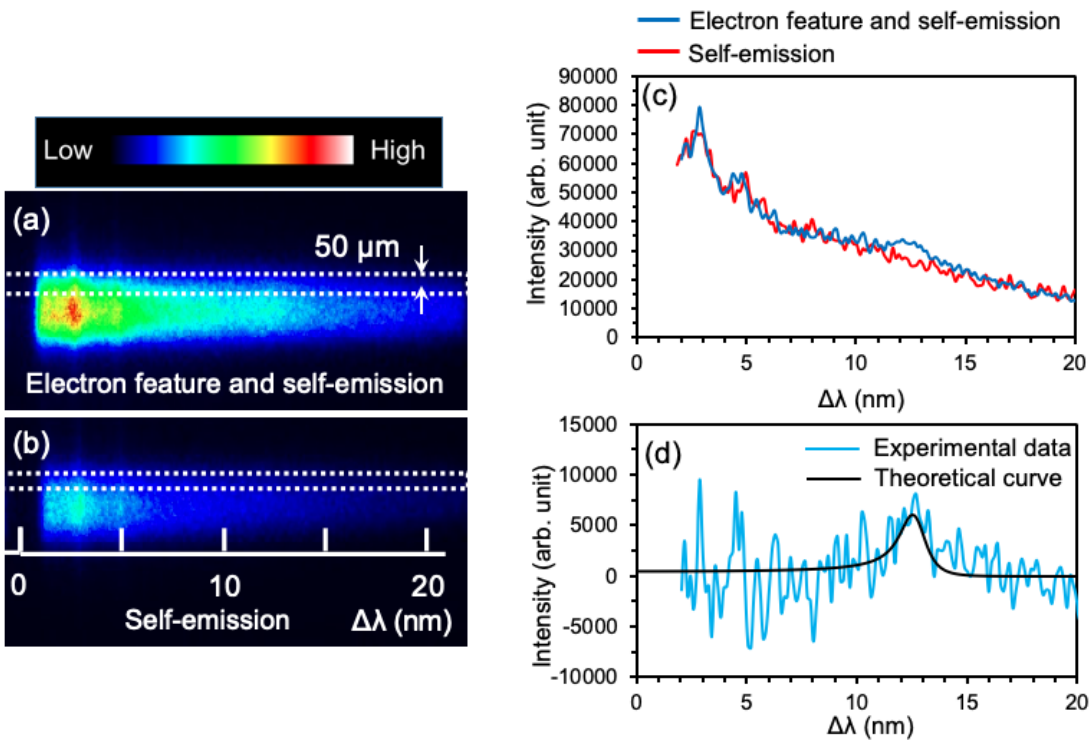

Fig. 4.5 Images of (a) the electron feature and the self-emission, and (b) the self-emission. (c) Spectra extracted from (a) and (b). (d) Spectrum of the electron feature.

References

[1] T. Morita, Y. Sakawa, K. Tomita, T. Ide, Y. Kuramitsu, K. Nishio, K. Nakayama, K. Inoue, T. Moritaka, H. Ide, M. Kuwada, K. Tsubouchi, K. Uchino, and H. Takabe, Phys. Plasmas 20, 092115 (2013).

[2] E. R. Kieft, J. J. A. M. van der Mullen, G. M. W. Kroesen, V. Banine, and K. N. Koshelev, Phys. Rev. E 70, 056413 (2004).

[3] E. R. Kieft, J. J. A. M. van der Mullen, and V. Banine, Phys. Rev. E **72**, 026415 (2005).

[4] S. Hassaballa, M. Yakushiji, Y. K. Kim, K. Tomita, K. Uchino and K. Muraoka, IEEE Trans. Plasmas Sci., vol. 32, p. 127, (2004).

[5] A. Kono and K. Nakatani, Rev. Sci. Instrum., vol. 71, no. 7, p. 2716, (2000).

[6] K. Tomita, S. Hassaballa, and K. Uchino: Denki Gakkai Ronbunshi A 130 (2010) 1099 [in Japanese].

[7] H. J. Kunze: Z. Naturforsch. A 20, 801 (1965).

[8] Bentley R E, J. Phys. D: Appl. Phys. **30**, 2880 (1997).

[9] Murphy A B, Phys. Rev. Lett. **89,** 025002 (2002).

Chapter 5

Conclusion

The research described in this thesis was aimed at the development and application of laser Thomson scattering (LTS) system suitable for EUV light source plasmas. EUV light source plasma parameters such as electron density (n_e), electron temperature (T_e), and averaged ionic charge (Z) were measured by detecting ion feature of collective Thomson scattering. T_e was assumed equal to ion temperature (T_i). There was no previous research realized the diagnostic of EUV light source with high conversion efficiency (CE), and this result clarified the spatial structure of EUV light source for the first time. In addition, we achieved simultaneous detections of the ion feature and the electron feature to measure the four parameters without any assumption. The results obtained by this study are summarized below.

I. A diagnostic method for EUV light source plasmas using LTS technique was developed. Concerning T_e, the lower detection limit of ~10 eV has been achieved by using a spectrometer which was developed to have 12 pm spectral resolution and sufficient stray light rejection (~10^{-4}) at ±14 pm from λ_0. The spatial resolutions of the measurements were 13, 50, and 20 μm for the x, y, and z axis directions respectively.

II. It was performed that direct measurements of the spatial distributions of n_e, T_e, and Z of EUV light source plasmas, whose CEs are 2.8–4.0%. From the LTS measurements, it becomes possible to compare the EUV emission profiles with the plasma parameters directly, for the first time. The results clearly show that intense EUV emissions were obtained from the positions where the plasma conditions are adequate for EUV emissions, which are predicted by previous simulation studies.

III. The detailed measurements of the ion feature spectra resulted in the time-resolved two-dimensional spatial profiles of n_e, T_e, and Z. The two-dimensional plasma profiles of the electron density and temperature significantly changed with the delay time between the pre-pulse and main lasers; and an electron density of $(4–8) \times 10^{24}$ m^{-3} and an electron temperature of ≥ 25 eV were simultaneously observed for the highest CE in the large plasma volume.

IV. The whole spectrum including the ion feature and the electron feature of collective Thomson scattering from laser-produced tin plasmas for EUV light sources has been observed for the first time. The purpose is to realize the evaluation of the n_e, T_e, T_i, and Z without any assumptions. Since the intensity of the electron feature is very weak compared with self-emissions from the plasma, efforts were concentrated to detect the peak wavelength of the electron feature. By applying the spectrometer system appropriately designed and optimizing the scattering geometry, it was achieved to detect the peak of the electron feature with the signal-to-noise ratio larger than one.

In this study, EUV light source plasmas were diagnosed using LTS technique and confirmed that the plasma volume with electron density (4–8) × 10^{24} m^{-3} and temperature ≥25 eV gave a high CE. We believe that these straightforward measurements of plasma parameters are very useful for further understanding and optimization of laser-produced plasma EUV light sources and will lead further improvements toward a higher CE in the future.

Acknowledgements

First of all, I would like to express my deepest gratitude to my advisor, Professor Kiichiro Uchino, for giving me the great opportunity of joining the PhD course in Kyushu University, for his excellent guidance, caring, patience and providing me with an excellent atmosphere for doing research. Also I would like to express my sincere appreciation to Associate Professor Yukihiko Yamagata for guidance, active help, discussion, and encouragement on my research

I would like to express my deepest appreciate to Assistant Professor Kentaro Tomita for his precious comments, discussion, and shared his great experience of laser Thomson scattering technique. Without his help I would not be able to do any experiment in laboratory.

My sincere thanks also go to my defense committee: Professor Reiji Hattori and Professor Naoji Yamamoto for careful reading my thesis and their valuable comments and suggestions.

I would like to thank the previous and current colleagues and members of the laboratory, who always supported and encouraged me with providing warm atmosphere during my research. I especially thank Ryo Shimoda, Kazutaka Nishikawa, Toshiaki Eguchi, Syoichi Tsukiyama, Raimu Fukada, Fumitaka Ito, and Yuki Fukushige. I also would like to thank the Yumi Sakuragi who supported me with the office work.

Financial supports from Green Asia program of Kyushu University and Grant-in-Aid for JSPS Research Fellow are greatly appreciated. These supports enable me to focus on my research and study.

Finally, I would like to thank my family, Chidori Sato, Nami Takayama, Kanata Takayama, and Naomi Sato. They were always supporting and encouraging me with their best wishes. I would like to dedicate this thesis to them.